Exclusive semileptonic $B_s \to K\ell\nu$ decays on the lattice

J. M. Flynn,[1,2,†] R. C. Hill,[3,‡] A. Jüttner,[1,4,2,‖] A. Soni,[5,§] J. T. Tsang,[4,*] and O. Witzel[6,¶]

(RBC/UKQCD)

[1]*Physics and Astronomy, University of Southampton, Southampton SO17 1BJ, United Kingdom*
[2]*STAG Research Centre, University of Southampton, Southampton SO17 1BJ, United Kingdom*
[3]*School of Physics and Astronomy, University of Edinburgh, Edinburgh EH9 3FD, United Kingdom*
[4]*Theoretical Physics Department, CERN, Geneva, Switzerland*
[5]*Physics Department, Brookhaven National Laboratory, Upton, New York 11973, USA*
[6]*Center for Particle Physics Siegen, Theoretische Physik 1, Naturwissenschaftlich-Technische Fakultät, Universität Siegen, 57068 Siegen, Germany*

(Received 2 April 2023; accepted 25 May 2023; published 16 June 2023)

Semileptonic $B_s \to K\ell\nu$ decays provide an alternative b-decay channel to determine the Cabibbo-Kobayashi-Maskawa (CKM) matrix element $|V_{ub}|$ and to obtain a R-ratio to investigate lepton-flavor-universality violations. Results for the CKM matrix element may also shed light on the discrepancies seen between analyses of inclusive or exclusive decays. We calculate the decay form factors using lattice QCD with domain-wall light quarks and a relativistic b-quark. We analyze data at three lattice spacings with unitary pion masses down to 268 MeV. Our numerical results are interpolated/extrapolated to physical quark masses and to the continuum to obtain the vector and scalar form factors $f_+(q^2)$ and $f_0(q^2)$ with full error budgets at q^2 values spanning the range accessible in our simulations. We provide a possible explanation of tensions found between results for the form factor from different lattice collaborations. Model- and truncation-independent z-parametrization fits following a recently proposed Bayesian-inference approach extend our results to the entire allowed kinematic range. Our results can be combined with experimental measurements of $B_s \to D_s$ and $B_s \to K$ semileptonic decays to determine $|V_{ub}| = 3.8(6) \times 10^{-3}$. The error is currently dominated by experiment. We compute differential branching fractions and two types of R ratios, the one commonly used as well as a variant better suited to test lepton-flavor universality.

DOI: 10.1103/PhysRevD.107.114512

I. INTRODUCTION

High-precision tests of the Standard Model (SM) from flavor physics are an important complement to direct searches at colliders for new physics. The absence of tree-level flavor-changing neutral currents in the SM provides one window where new physics effects could be seen, though it is important to test high-precision calculations of both tree- and loop-level SM processes against experiment.

New physics is expected to occur at higher energy scales, and seeing its effects is more likely if the decaying particle can release large amounts of energy. Decays of mesons containing a heavy b-quark provide many opportunities because the b-quark lives long enough for experimental investigation but also delivers more than 4 GeV of energy. The large b-quark mass allows a plethora of decay channels and correspondingly many tests of the SM. Tantalizing deviations between SM predictions and experimental measurements have been reported [1–6]. While the latest experimental LHCb results [7] confirm the universality of lepton families under the weak interaction, the high-energy reach of flavor physics continues to make it a primary probe for the search of beyond-SM physics.

Here, we focus on B_s-meson decay arising at tree level in the SM with a kaon in the final state. Lattice results over the full q^2 range for $B_s \to K\ell\nu$ form factors have been obtained by HPQCD [8,9], RBC-UKQCD [10], and

*Corresponding author.
j.t.tsang@cern.ch
†j.m.flynn@soton.ac.uk
‡ryan.hill@ed.ac.uk
‖andreas.juttner@cern.ch
§adlersoni@gmail.com
¶oliver.witzel@uni-siegen.de

Fermilab-MILC [11] as well as at a single q^2 value by the Alpha Collaboration [12]. Recent lattice results for $B_s \to K\ell\nu$ semileptonic decays are summarized in Refs. [13–15].

$B_s \to K\ell\nu$ decays have been observed by LHCb [16] and can be used to obtain the magnitudes of the CKM matrix elements $|V_{ub}|$. Using these alternative b-decay channels may shed light on the use of different kinematical parametrizations for the exclusive decay form factors and on tensions within and between extractions of $|V_{ub}|$ from inclusive or exclusive decays.

The remainder of this paper is structured as follows. In Sec. II, we describe the form factors we will compute and provide the details of our lattice computation. In Sec. III, we describe the statistical analysis of the lattice data. In Sec. IV, we determine estimates for all sources of uncertainties and thereby assemble a complete error budget. Section V discusses the extrapolation of the obtained form factors over the full kinematical range and provides a wealth of quantities of phenomenological interest before we conclude in Sec. VI.

II. LATTICE CALCULATION

A. Form factors

We work in the B_s-meson rest frame for our calculations. For $\bar{B}_s^0 \to K^+\ell^-\bar{\nu}_\ell$, the differential decay rate in this frame is given by

$$\frac{d\Gamma(B_s \to K\ell\nu)}{dq^2} = \eta_{\rm EW}\frac{G_F^2|V_{ub}|^2}{24\pi^3}\frac{(q^2-m_\ell^2)^2|\mathbf{p}_K|}{(q^2)^2} \times\left[\left(1+\frac{m_\ell^2}{2q^2}\right)|\mathbf{p}_K|^2|f_+(q^2)|^2 + \frac{3m_\ell^2}{8q^2}\frac{(M_{B_s}^2-M_K^2)^2}{M_{B_s}^2}|f_0(q^2)|^2\right]. \quad (1)$$

The 4-momenta of the B_s and the final-state kaon are denoted by p_{B_s} and p_K, respectively. M_{B_s} and M_K denote the corresponding meson masses, E_K is the K-meson energy, $|\mathbf{p}_K| = (E_K^2 - M_K^2)^{1/2}$, and $q = p_{B_s} - p_K$ is the momentum transfer between the B_s and K mesons. $\eta_{\rm EW}$ is an electroweak correction factor.[1] The form factors f_+ and f_0 arise in the decomposition of the QCD matrix element

$$\langle K(p_K)|\mathcal{V}^\mu|B_s(p_{B_s})\rangle = f_+(q^2)\left(p_K^\mu + p_{B_s}^\mu - q^\mu\frac{M_{B_s}^2-M_K^2}{q^2}\right) + f_0(q^2)\frac{M_{B_s}^2-M_K^2}{q^2}q^\mu. \quad (2)$$

[1]We follow Ref. [17] and take $\eta_{\rm EW} = 1.011(5)$ by combining the factor computed by Sirlin [18] with an estimate of final-state electromagnetic corrections using the ratio of signal yields from charged and neutral decay channels.

In the SM, $\mathcal{V}^\mu = \bar{u}\gamma^\mu b$ is the continuum charged current operator. For lattice simulations, it is convenient to use the alternative parametrization

$$\langle K|\mathcal{V}^\mu|B_s\rangle = \sqrt{2M_{B_s}}[v^\mu f_\cdot(E_K) + p_\perp^\mu f_\perp(E_K)], \quad (3)$$

and the relations

$$f_0(q^2) = \frac{\sqrt{2M_{B_s}}}{M_{B_s}^2-M_K^2}[(M_{B_s}-E_K)f_\parallel(E_K) + (E_K^2-M_K^2)f_\perp(E_K)], \quad (4)$$

$$f_+(q^2) = \frac{1}{\sqrt{2M_{B_s}}}[f_\parallel(E_K) + (M_{B_s}-E_K)f_\perp(E_K)], \quad (5)$$

where v is the B_s meson 4-velocity, $(p_{B_s})_\perp^\mu \equiv p_K^\mu - (p_K\cdot v)v^\mu$, and in the B_s meson rest frame

$$f_\parallel(E_K) = \frac{\langle K|\mathcal{V}^0|B_s\rangle}{\sqrt{2M_{B_s}}}, \quad f_\perp(E_K) = \frac{1}{p_K^i}\frac{\langle K|\mathcal{V}^i|B_s\rangle}{\sqrt{2M_{B_s}}}. \quad (6)$$

We note that no Einstein summation convention is applied in the second equation; it holds component by component for the nonzero components of p_K^i.

B. Action and parameters

Our calculations are based on a subset of RBC-UKQCD's $2+1$ flavor domain-wall fermion and Iwasaki gauge-field ensembles [19–22] which we summarize in Table I. Our dataset includes six ensembles at three different lattice spacings, with pion masses down to 268 MeV. Light and strange quarks are simulated using domain-wall fermions [23–28]. The light (up and down) sea-quark masses are degenerate and correspond to pion masses in the range 268 MeV $\le M_\pi \le$ 434 MeV. The strange sea-quark mass is within 20% to 25% of its physical value on the C and M ensembles and is tuned to a deviation of 1% on the F1S ensemble.

Bottom quarks are simulated using the relativistic heavy-quark (RHQ) action [30,31], a variant of the Fermilab action [32] with three nonperturbatively tuned parameters [33]. The RHQ tuning procedure uses the experimentally measured B_s-meson mass and hyperfine splitting, together with the constraint that the lattice rest mass (measured from the exponential decay of meson correlation functions) equals the kinetic mass (measured from the meson dispersion relation) in order to determine these three parameters, in particular the bare quark mass ($m_0 a$), the clover coefficient (c_P) and the anisotropy parameter (ζ). The outputs of the RHQ tuning for the ensembles used here are given in Table XVII, with details of the procedure in Appendix A.

Light and strange quarks are generated using point sources, whereas b-quarks are generated using a Gaussian

TABLE I. RBC/UKQCD coarse (C), medium (M), and fine (F) gauge-field ensembles [19–22] used in this calculation, with 2 + 1-flavor domain-wall fermions and Iwasaki-gauge action. The domain-wall height for light and strange quarks is $M_5 = 1.8$. The ensembles are generated using the Shamir domain-wall kernel [23,24]. am_l denotes the light sea-quark mass, and $am_s^{\rm sea}$ denotes the strange sea-quark mass. The lattice spacing and physical strange quark were obtained in the combined analysis of Refs. [21,22,29]. The valence strange-quark masses used in our simulations on the C(M) ensembles are $am_s^{\rm sim} = 0.03224(0.025)$, while on F1S, we used $am_s^{\rm sim} = am_s^{\rm sea}$.

	L/a	T/a	L_s	a^{-1}/GeV	am_l	$am_s^{\rm sea}$	$am_s^{\rm phys}$	M_π/MeV	# configurations	# sources
C1	24	64	16	1.7848(50)	0.005	0.040	0.03224(18)	340	1636	1
C2	24	64	16	1.7848(50)	0.010	0.040	0.03224(18)	434	1419	1
M1	32	64	16	2.3833(86)	0.004	0.030	0.02477(18)	301	628	2
M2	32	64	16	2.3833(86)	0.006	0.030	0.02477(18)	363	889	2
M3	32	64	16	2.3833(86)	0.008	0.030	0.02477(18)	411	544	2
F1S	48	96	12	2.785(11)	0.002144	0.02144	0.02167(20)	268	98	24

smeared source [34,35] in order to reduce excited-state contamination. We use the smearing parameters that were determined in Ref. [33] and list them in Table XIII in Appendix A.

Our data are generated using the lattice QCD software packages QLUA [36] and CHROMA [37]. Further details of the setup can be found in Refs. [10,22,29,38,39].

C. Operator renormalization and improvement

Matrix elements from our simulations are matched to continuum ones using the relation

$$\langle K|\mathcal{V}_\mu|B_s\rangle = Z_{V_\mu}^{bl}\langle K|V_\mu|B_s\rangle, \tag{7}$$

where l stands for the light quark and we denote the continuum and lattice currents by $\mathcal{V}_\mu$ and V_μ, respectively. The renormalization factor

$$Z_{V_\mu}^{bl} = \rho_{V_\mu}^{bl}\sqrt{Z_V^{ll}Z_V^{bb}} \tag{8}$$

is obtained following Refs. [40,41]. The flavor-conserving renormalization factors Z_V^{ll} and Z_V^{bb} account for most of the operator renormalization, while $\rho_{V_\mu}^{bl}$ is a residual correction, expected to be close to unity because most of the radiative corrections, including tadpoles, cancel [42]. We obtain Z_V^{bb} nonperturbatively from the matrix element of the $b \to b$ vector current between two B_s mesons:

$$Z_V^{bb}\langle B_s|V_0|B_s\rangle = 2M_{B_s}. \tag{9}$$

Details of the calculation are given in appendix A of Ref. [38]. The light-light renormalization factor was calculated from Z_A^{ll} [20] using the relation $Z_V^{ll} = Z_A^{ll}$ to $O(am_{\rm res})$ for domain-wall fermions.

Following our previous work [10], we improve the heavy-light vector current to $O(\alpha_s a)$ using the following operators,

$$V_0^{\rm imp}(x) = V_0^0(x) + c_t^3 V_0^3(x) + c_t^4 V_0^4(x), \tag{10}$$

$$V_i^{\rm imp}(x) = V_i^0(x) + c_s^1 V_i^1(x) + c_s^2 V_i^2(x) + c_s^3 V_i^3(x) + c_s^4 V_i^4(x), \tag{11}$$

where c_t^n and c_s^n are coefficients and

$$V_\mu^0(x) = \bar\psi(x)\gamma^\mu Q(x), \tag{12}$$

$$V_\mu^1(x) = \bar\psi(x)2\vec{D}_\mu Q(x), \tag{13}$$

$$V_\mu^2(x) = \bar\psi(x)2\overleftarrow{D}_\mu Q(x), \tag{14}$$

$$V_\mu^3(x) = \bar\psi(x)2\gamma_\mu\gamma_i\vec{D}_i Q(x), \tag{15}$$

$$V_\mu^4(x) = \bar\psi(x)2\gamma_\mu\gamma_i\overleftarrow{D}_i Q(x), \tag{16}$$

with ψ a light quark and Q an RHQ quark. The covariant derivatives are given by

$$\vec{D}_\mu Q(x) = \frac{1}{2}(U_\mu(x)Q(x+\hat\mu) - U_\mu^\dagger(x-\hat\mu)Q(x-\hat\mu)), \tag{17}$$

$$\bar\psi(x)\overleftarrow{D}_\mu = \frac{1}{2}(\bar\psi(x+\hat\mu)U_\mu^\dagger(x) - \bar\psi(x-\hat\mu)U_\mu(x-\hat\mu)). \tag{18}$$

Both the residual renormalization factor ρ_V^{bl} and the coefficients c_t^n and c_s^n were computed at one-loop order [43] in mean-field improved lattice perturbation theory [44], with the results given in Table XX in Appendix C.

D. Setup of the calculation

In Fig. 1, we sketch our calculation of three-point correlation functions using sequential propagators separating initial and final state by Δ_t [45]. The initial B_s meson is located at $t_{\rm snk} = t_{\rm src} + \Delta_t$, whereas the final-state kaon is at $t_{\rm src}$. We proceed by letting the strange spectator quark propagate from $t = t_{\rm src}$ to $t = t_{\rm snk}$ where we give it a sink which is turned into the sequential source for the parent

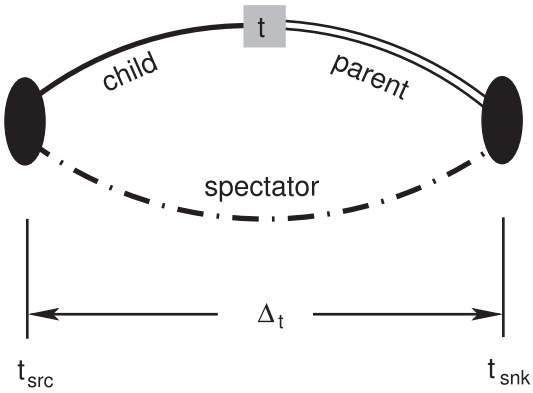

FIG. 1. Sketch of the construction of the three-point function in the "forward direction." The strange spectator quark (dot-dashed line) originates from time slice $t_{\rm src}$ and propagates forward to time slice $t_{\rm snk}$ where we create a point sink and turn it into a sequential source for the parent b-quark (double line) propagating backward. This sequential propagator is contracted with the child light quark (solid line) also originating from $t_{\rm src}$. The contraction of child and parent quark (gray box) is calculated inserting the operators for the vector current and varied over the time slices $t_{\rm src}$ to $t_{\rm snk}$.

b-quark. The b-quark is contracted with a child light quark also starting at $t = t_{\rm src}$ over all time slices in the range $t_{\rm src} \le t \le t_{\rm snk}$. The contraction is calculated inserting the operators for the vector current defined in Eqs. (12)–(16). In addition to the shown setup in the "forward" direction, we effectively double statistics by calculating the "backward" direction; i.e., we use a second sink location at $t'_{\rm snk} = t_{\rm src} - \Delta_t$. For each configuration, we first average forward and backward three-point correlators before proceeding with the analysis. This step is similar to "folding" two-point correlators about the central time slice in order to take advantage of the symmetry of forward- and backward-propagating states.

We use one time source at $t_{\rm src}/a = 0$ for the coarse C1 and C2 ensembles; two time sources at $t_{\rm src}/a = 0$, 32 for the medium M1, M2, and M3 ensembles; and 24 time sources separated by four time slices on the F1S ensemble. The separation Δ_t on ensembles C1, C2, M1, M2, and M3 is the same as in our previous work [10] where we carefully studied several source-sink separations to cleanly identify the ground-state signal. On the F1S ensemble, we generated data for multiple source-sink separations ($\Delta_t/a = 30$, 32, 34) to study the effects of excited states. We found that the signal saturates for $\Delta_t/a = 32$ with the center of the signal region being ground-state dominated and compatible with the $\Delta_t/a = 34$ dataset. We therefore chose $\Delta_t/a = 32$ for our final analysis. Our choice of $\Delta_t/a = 20$, 26, and 32 for the three lattice spacings corresponding to the C, M, and F ensembles, respectively, results in a Δ_t that is nearly constant in physical units. In order to further decorrelate measurements, we perform a random 4-vector shift on the gauge field prior to placing any source. This 4-vector shift is equivalent to randomly choosing the first source position on each configuration but simplifies the bookkeeping.

The initial B_s meson is kept at rest, and momentum is inserted in the final state through the current operator. The simulations use strange spectator quarks with a mass close to the physical value (see Table I), and we tune the RHQ parameters such that the parent quark corresponds to a physical b quark. The child light quark is unitary and has the same mass as the light sea quarks.

III. ANALYSIS

The analysis to extract form factor results is implemented ensemble by ensemble as a simultaneous correlated frequentist fit over two-point and three-point correlation functions to obtain masses and the lattice form factors $f_\parallel$ and $f_\perp$ for all simulated momentum transfers, i.e., one single fit per ensemble. These form factors are then renormalized and converted to f_+ and f_0 using Eqs. (4) and (5). They are subsequently interpolated/extrapolated to physical quark masses and to the continuum limit in a single step. We use bootstrap resampling [46] with 1000 samples.

A. Two-point correlation function fits

Here, we describe individual correlated fits to the π, K, and B_s two-point data. The results for the pion mass determined here will enter subsequent analyses. For K and B_s, this section only serves to determine optimal fit ranges, which we use in the next section for the combined fit with ratios of three-point and two-point correlators.

The functional form of the two-point correlation functions C_2 is given by

$$\begin{aligned} C_2^P(t, T, \mathbf{p}_P) &= \sum_{\mathbf{x}} e^{i\mathbf{p}_P\cdot\mathbf{x}} \langle \mathcal{O}_{\rm snk}(\mathbf{x}, t)\mathcal{O}^\dagger_{\rm src}(\mathbf{0}, 0)\rangle \\ &= \sum_{n=0}^{N} \langle 0|\mathcal{O}_{\rm snk}|X^{(n)}\rangle\langle X^{(n)}|\mathcal{O}^\dagger_{\rm src}|0\rangle \\ &\quad \times \left(\frac{e^{-E_{P,n}t} + e^{-E_{P,n}(T-t)}}{2E_{P,n}}\right), \end{aligned} \tag{19}$$

where the interpolating operators $\mathcal{O}_{\rm src}$ and $\mathcal{O}_{\rm snk}$ are given by $\bar{l}\gamma^5 l$, $\bar{s}\gamma^5 l$, and $\bar{b}\gamma^5 s$ and are chosen to induce states with the quantum numbers of the π, K, and B_s, respectively.

In a first step, we extract the energies $E_{P,n}$ and amplitudes $\langle X^{(n)}|\mathcal{O}|0\rangle$ for $n = 0, 1$ separately for the π, K, and B_s meson by fitting the correlation functions to the functional form given in Eq. (19) with $N = 1$. For the B_s mesons, we simultaneously fit the smeared-sink and point-sink correlation functions under the constraint that they both describe the same meson energy. The fit ranges are determined in such a way that the inclusion of the ground and excited states visibly describes the data well, while also providing

an acceptable p-value. Furthermore, we check that the results are stable under variations of the fit range.

The energies of the final-state kaon can be related to its rest mass via the continuum ($E_K^2 = M_K^2 + \mathbf{p}_K^2$) or the lattice dispersion relation,

$$\sinh^2\left(\frac{aE_K(aM_K, a\mathbf{p}_K)}{2}\right) = \sinh^2\left(\frac{aM_K}{2}\right) + \sum_{i=1}^{3}\sin^2\left(\frac{ap_{K,i}}{2}\right). \tag{20}$$

We have tested that the data are described by the dispersion relation using lattice momenta $\mathbf{p}_K = 2\pi\mathbf{n}/L$ with $\mathbf{n}^2 = 0$, 1, 2, 3, 4, where equivalent 3-momenta are averaged. This justifies imposing the lattice dispersion relation in the combined fit that we will describe in the next section. We will also compare these results with those based on the continuum dispersion relation in order to assess systematic effects.

B. Form factors from global fits

Without loss of generality, we assume $t_{\mathrm{src}} = 0$ in the following. The three-point correlation functions for the transition $B_s \to K$ have the functional form

$$\begin{aligned} C_{3,\mu}(t, \Delta_t, \mathbf{p}_K) &= \sum_{\mathbf{x},y} e^{i\mathbf{p}_K\cdot\mathbf{y}}\langle \mathcal{O}_{B_s}(\mathbf{x}, \Delta_t) V_\mu^{\mathrm{imp}}(\mathbf{y}, t)\mathcal{O}_K^\dagger(\mathbf{0}, 0)\rangle \\ &= \sum_{n,m}\langle 0|\mathcal{O}_{B_s}|B_s^{(n)}\rangle\langle B_s^{(n)}|V_\mu^{\mathrm{imp}}|K^{(m)}\rangle\langle K^{(m)}|\mathcal{O}_K^\dagger|0\rangle \\ &\quad\times\frac{e^{-E_{K,m}t}e^{-M_{B_s,n}(\Delta_t - t)}}{4E_{K,m}M_{B_s,n}}, \end{aligned} \tag{21}$$

where V_μ^{imp} are the improved lattice temporal and spatial vector currents from Eqs. (10) and (11). We notice that our notation suppresses the fact that the operators inducing the B_s mesons can be either smeared or local at the sink. Furthermore, we neglect around-the-world effects due to the finite temporal extent T as these are suppressed by $e^{-E_K(T-\Delta_t)}$.

To determine the form factors $f_\parallel$ and $f_\perp$ [compare Eq. (6)], we require the ground-state matrix element $\langle K|V_\mu^{\mathrm{imp}}|B_s\rangle$ [where for convenience we dropped the superscript (0)]. To this end, we define the ratio $R_{3,\mu}(t, t_{\mathrm{snk}}, \mathbf{p}_K)$ as

$$\begin{aligned} R_{3,\mu}(t, t_{\mathrm{snk}}, \mathbf{p}_K) &= \frac{C_{3,\mu}(t, t_{\mathrm{snk}}, \mathbf{p}_K)}{\sqrt{C_2^K(t, \mathbf{p}_K)C_2^{B_s}(t_{\mathrm{snk}} - t, \mathbf{0})}} \\ &\quad\times\sqrt{\frac{2E_{K,0}}{e^{-E_{K,0}t - M_{B_s,0}(t_{\mathrm{snk}} - t)}}}, \end{aligned} \tag{22}$$

where we ensure that the appropriate smearing is used to cancel the overlap factors between the three-point and two-point correlation functions. By construction, these ratios satisfy

$$\begin{aligned} f_\parallel^{\mathrm{bare}}(\mathbf{p}_K) &= \lim_{0\ll t\ll t_{\mathrm{snk}}} R_{3,0}(t, t_{\mathrm{snk}}, \mathbf{p}_K) \\ f_\perp^{\mathrm{bare}}(\mathbf{p}_K) &= \lim_{0\ll t\ll t_{\mathrm{snk}}} \frac{1}{p_K^i} R_{3,i}(t, t_{\mathrm{snk}}, \mathbf{p}_K), \end{aligned} \tag{23}$$

so we can obtain the form factors $f_\parallel^{\mathrm{bare}}$ and $f_\perp^{\mathrm{bare}}$ by fitting the ratio $R_{3,\mu}$.

In practice, we carry out a simultaneous correlated fit over the point-point K and smeared-point and point-point B_s two-point functions (including one excited state in both cases), together with all components μ of the three-point correlation functions. For the latter, we simultaneously fit over results for all momenta including ground-state-B_s-to-excited-K and excited-B_s-to-ground-state-K terms for the matrix element of the current. Throughout this fit, we enforce the lattice dispersion relation to describe the energy levels of the kaon [cf. Eq. (20)]. Except for the results on F1S, for momenta $\mathbf{n}^2 = 3$, 4, the statistical noise on the three-point functions is too large to allow for meaningful constraints on the latter matrix element, and we do not include it in the fit. The term containing both the B_s and K excited states leads to poorly constrained fits and is excluded. The inclusion of excited states allows us to extend the range of time slices we can fit, as illustrated in Fig. 2. In order to limit the impact of strong correlations between neighboring time slices in the ratio $R_{3,\mu}$ only every fourth time slice enters the fit. We choose fit ranges which visibly describe the data well while still giving acceptable p-values. The results for the ground-state matrix elements determined in this way show no dependence on the choice of lower and upper end of the fit range for the ratio when varied by ± 1 time slices. An example for this fit is shown in Fig. 2.

What remains is to extract Z_V^{bb}. We first consider the temporal component of the zero-momentum matrix element for the $b \to b$ vector current on the B_s meson and restrict ourselves to the region where only the ground state contributes:

$$\begin{aligned} C_{3,0}(t, t_{\mathrm{snk}}, \mathbf{0}) &= \lim_{0\ll t\ll t_{\mathrm{snk}}}\sum_{\mathbf{x},\mathbf{y}}\langle \mathcal{O}_{B_s}(\mathbf{x}, t_{\mathrm{snk}})V_0^{bb}(\mathbf{y}, t)\mathcal{O}_{B_s}^\dagger(\mathbf{0}, 0)\rangle \\ &= \frac{|\langle 0|\mathcal{O}_{B_s}|B_s\rangle|^2}{4M_{B_s}^2}\langle B_s|V_0^{bb}|B_s\rangle e^{-M_{B_s}t_{\mathrm{snk}}}. \end{aligned} \tag{24}$$

Recalling Eq. (9), we notice that dividing the two-point function $C_2^{B_s}$ at $t = t_{\mathrm{snk}}$ (with the appropriate smearing) by this expression gives

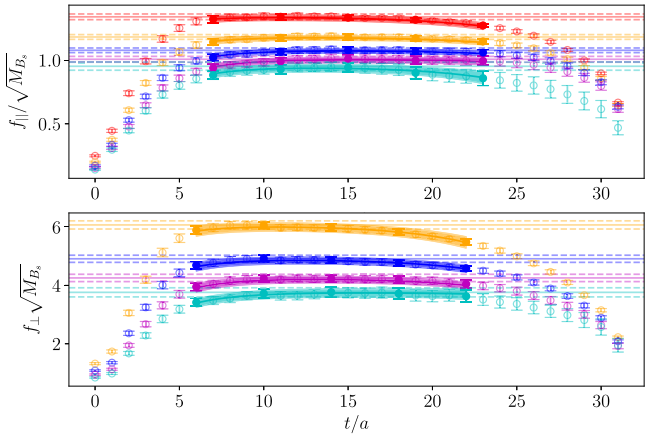

FIG. 2. Example extraction of $f_\parallel$ (top) and $f_\perp$ (bottom) on the F1S ensemble from a correlated global fit. The different colors are for different momenta $\mathbf{n}2\pi/L$ injected at the current. The plot shows the fit including excited-state contributions as well as the ground-sate contribution (horizontal dashed lines). Filled symbols indicate the points that were included in the fits.

$$\frac{C_2^{B_s}(t_{\rm snk},T,\mathbf{0})}{C_{3,0}(t,t_{\rm snk},\mathbf{0})} = \lim_{0\ll t\ll t_{\rm snk}} \frac{2M_{B_s}}{\langle B_s|V_0^{bb}|B_s\rangle} = Z_V^{bb}, \quad (25)$$

allowing us to extract Z_V^{bb} from a simple fit to a constant. We show data and the fit on the F1S ensemble in Fig. 3 and collect results for all ensembles in Table II.

With the value of Z_V^{bb} at hand, and using Eq. (8), we can determine the renormalization constants $Z_{V_\mu}^{bl}$ and compute

$$f_\parallel(\mathbf{p}_P) = Z_{V_0}^{bl} f_\parallel^{\rm bare}(\mathbf{p}_P),$$
$$f_\perp(\mathbf{p}_P) = Z_{V_i}^{bl} f_\perp^{\rm bare}(\mathbf{p}_P). \quad (26)$$

Finally, we convert to $f_0(q^2)$ and $f_+(q^2)$ using Eqs. (4) and (5). Table III summarizes all fit results.

C. Chiral-continuum extrapolation

We extrapolate the renormalized lattice form factors to vanishing lattice spacing and to the physical light-quark mass and interpolate in the kaon energy, using

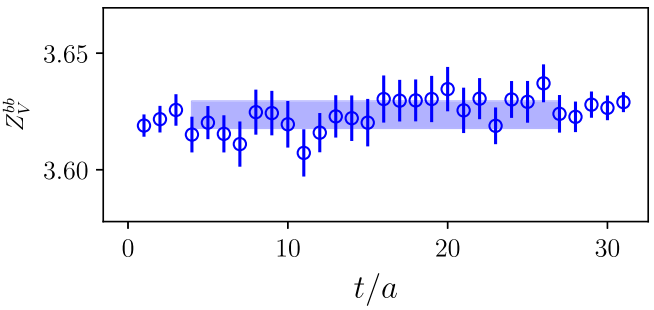

FIG. 3. Example extraction of the vector-current renormalization constant Z_V^{bb} on the F1S ensemble.

next-to-leading order (NLO) SU(2) chiral perturbation theory for heavy-light mesons (HMχPT) in the "hard-pion" (or in this case kaon) limit [47–49]. In the SU(2) theory, the strange quark is integrated out. The chiral logarithms for $B_s \to K\ell\nu$ depend on the pion mass and the kaon energy, while the SU(2) low-energy constants depend implicitly on the values of the strange-quark and b-quark masses. The function we use is

$$f_X^{B_s\to K}(M_\pi, E_K, a^2) = \frac{\Lambda}{E_K+\Delta_X}\left[c_{X,0}\left(1+\frac{\delta f(M_\pi^s)-\delta f(M_\pi^p)}{(4\pi f_\pi)^2}\right) + c_{X,1}\frac{\Delta M_\pi^2}{\Lambda^2} + c_{X,2}\frac{E_K}{\Lambda} + c_{X,3}\frac{E_K^2}{\Lambda^2} + c_{X,4}(a\Lambda)^2\right], \quad (27)$$

where $X = +, 0$ for the vector and scalar form factor, respectively, and where M_π^s is the simulated pion mass on a given ensemble; $M_\pi^p = (2M_{\pi^\pm} + M_{\pi^0})/3$ is the isospin-averaged physical pion mass; $\Delta M_\pi^2 = (M_\pi^s)^2 - (M_\pi^p)^2$; and $\Lambda = 1$ GeV is the renormalization scale appearing in the one-loop chiral logarithm in δf shown in (28) below and is also used as a dimensionful scale to render the fit coefficients dimensionless. $\Delta_X = M_{B^*} - M_{B_s}$, and the B^* is a $\bar{b}u$ flavor state with $J^P = 1^-$ for f_+, or $J^P = 0^+$ for f_0. For f_+, this is the vector meson B^* with mass $M_{B^*} = 5.32471(21)$ GeV [50], while for f_0, there is a theoretical estimate for the 0^+ state, $M_{B^*(0^+)} = 5.63$ GeV [51][2] (the formalism for effective theories for heavy hadrons of arbitrary spin was derived in Ref. [73] and is reviewed in Ref. [74]). We take $\Delta_+ = -42.1$ MeV for f_+ using experimentally measured masses [50,75] and $\Delta_0 = 263$ MeV for f_0 using the theoretical estimate from Ref. [51]. Since the estimated $B^*(0^+)$ pole location is rather far from the physical q^2 region, the fit is insensitive to its precise position (and varying it is included in our uncertainty for the chiral extrapolation).

While the 0^+ and 1^- poles describe the *physical* form factors f_0 and f_+, respectively, past work [10,11] used Eq. (27) for $f_\parallel$ and $f_\perp$ based on the observation in Eq. (4) that f_0 is dominated by $f_\parallel$ and f_0 by $f_\perp$. Below, we discuss whether this assumption is warranted with our data.

For the case of the f_+ form factor, the coefficient c_3 is compatible with zero within statistical errors. Since the quality of the fit remains good when removing this term from the ansatz, we perform the fits for f_+ without such a term.

The term δf entering (27) is the same for f_+ and f_0 and is given by

[2]Results from this and other theoretical calculations [52–71] are summarized in Table 4 of Ref. [72]. They span a range from 2% below to 2% above this value.

TABLE II. Numerical values of the renormalization constants Z_A^{ll} and Z_V^{bb}.

	C1	C2	M1	M2	M3	F1S
Z_A^{ll}	0.7172	0.7178	0.7449	0.7452	0.7452	0.7624
Z_V^{bb}	9.099(24)	9.135(23)	4.7767(87)	4.7602(75)	4.770(10)	3.6236(57)

TABLE III. Summary of results from the global fit and the separate fit to pion two-point functions. The squared momentum transfer, q^2, is determined from the outgoing kaon momentum, $\mathbf{k} = (2\pi/L)\mathbf{n}$, with the values of $|\mathbf{n}|^2$ being given in the table. The reduced χ^2 in the table is defined as $\chi^2_{\rm red} = \chi^2/N_{\rm dof}$.

	$\lvert\mathbf{n}\rvert^2$	C1	C2	M1	M2	M3	F1S
$N_{\rm dof}/\chi^2_{\rm red}/p$	–	41/1.35/0.06	54/0.95/0.59	41/0.93/0.61	46/1.27/0.10	51/1.24/0.11	57/0.77/0.90
$f_+(q^2)$	1	2.001(29)	2.011(27)	2.038(39)	1.995(28)	1.984(33)	2.355(50)
$f_+(q^2)$	2	1.545(29)	1.545(29)	1.578(40)	1.566(28)	1.561(33)	1.917(43)
$f_+(q^2)$	3	1.250(41)	1.270(38)	1.282(50)	1.288(33)	1.256(42)	1.663(43)
$f_+(q^2)$	4	1.029(65)	1.141(61)	1.040(75)	1.081(51)	1.055(61)	1.476(53)
$f_0(q^2)$	0	0.8710(93)	0.8872(97)	0.884(13)	0.8692(95)	0.877(12)	0.879(14)
$f_0(q^2)$	1	0.7523(93)	0.774(10)	0.769(14)	0.7442(93)	0.767(12)	0.796(12)
$f_0(q^2)$	2	0.672(13)	0.703(14)	0.699(18)	0.675(12)	0.690(14)	0.739(12)
$f_0(q^2)$	3	0.602(20)	0.662(22)	0.628(26)	0.633(19)	0.629(22)	0.703(16)
$f_0(q^2)$	4	0.581(36)	0.625(35)	0.564(42)	0.606(30)	0.558(37)	0.675(21)
aM_{B_s}	–	3.00572(97)	3.00977(88)	2.25278(88)	2.25186(70)	2.25321(80)	1.92574(87)
aM_K	–	0.30666(49)	0.32646(30)	0.22489(49)	0.23440(42)	0.24141(47)	0.19144(46)

	C1	C2	M1	M2	M3	F1S
$N_{\rm dof}/\chi^2_{\rm red}/p$	12/1.10/0.36	12/0.60/0.84	14/1.14/0.32	8/1.32/0.23	8/0.58/0.80	20/0.89/0.60
aM_π	0.19026(50)	0.24289(45)	0.12639(49)	0.15222(36)	0.17260(45)	0.09640(34)
M_π[GeV]	0.3395(13)	0.4335(15)	0.3012(16)	0.3628(16)	0.4114(18)	0.2684(14)

$$\delta f = -\frac{3}{4}\left(M_\pi^2 \log\left(\frac{M_\pi^2}{\Lambda^2}\right) + \frac{4M_\pi}{L}\sum_{|\mathbf{n}|\neq 0}\frac{K_1(|\mathbf{n}|M_\pi L)}{|\mathbf{n}|}\right). \quad (28)$$

The first term is the one-loop chiral logarithm, and the second term is an estimate for effects due to the finite (spatial) volume, where K_1 is a modified Bessel function of the second kind and $|\mathbf{n}|$ is the magnitude of a vector of integers $\mathbf{n} = (n_x, n_y, n_z)$ specifying the spatial lattice momentum $2\pi\mathbf{n}/L$. The second term is estimated using one-loop finite-volume SU(2) hard-pion χPT [76,77] where loop integrals are replaced by sums over lattice sites, with its expression derived in Ref. [78].

The pion masses entering the fit are obtained from separate two-point correlation function fits, and we take $f_\pi = 130.2$ MeV [79]. We include a term proportional to a^2 to account for the dominant lattice-spacing dependence. The domain-wall fermion and Iwasaki gluon actions are expected to have discretization errors $O((a\Lambda_{\rm QCD})^2)$, about 3% (5%) on the F (M) ensemble(s) for $\Lambda_{\rm QCD} = 500$ MeV, while power-counting estimates of errors in the RHQ action and heavy-light current are smaller, below 2%. The a^2 term in our fit therefore accounts for the leading discretization effects.

Results for the parameters of the chiral-continuum fit are given in Table IV. Figure 4 shows the fit, while the systematic errors from variations in the fit are discussed in Sec. IV and shown in Fig. 5. Values for the form factors in the continuum and physical quark mass limit, along with their statistical and systematic errors and correlations, are given at the end of the discussion of systematic errors in Sec. IV for a set of reference q^2 values. These are obtained by using the results in Table IV to evaluate the form factor for a given kaon energy, after setting $a = 0$, taking the limit $L \to \infty$ in Eqs. (27) and (28), and setting $m_\pi = (2m_\pi^\pm + m_\pi^0)/3 \approx 138$ MeV (isospin-averaged pion mass) [50].

IV. SYSTEMATIC ERROR ANALYSIS

Our systematic-error analysis has much in common with that done in our earlier work on semileptonic $B \to \pi\ell\nu$ and $B_s \to K\ell\nu$ decays [10]. We streamline our discussion where possible, relying on Ref. [10] for details, and introduce new features for this analysis.

TABLE IV. Fitted parameters for chiral-continuum extrapolation for the $B_s \to K\ell\nu$ form factors defined in (27). Results for the coefficients, statistical errors, and correlation matrix for the central continuum-limit fit. The fit quality is $(N_{\mathrm{dof}}/\chi^2_{\mathrm{red}}/p) = (20/1.09/0.35)$ for f_+ and $(25/1.12/0.11)$ for f_0.

			$c_{+,0}$	$c_{+,1}$	$c_{+,2}$	$c_{+,4}$	$c_{0,0}$	$c_{0,1}$	$c_{0,2}$	$c_{0,3}$	$c_{0,4}$
			1.8169	0.2803	−0.7542	−0.0936	0.5310	0.2273	0.2996	−0.0938	−0.0136
	$c^{+,0}$	$\delta c^{+,0}$	0.0453	0.2661	0.0411	0.1461	0.0269	0.1057	0.0748	0.0590	0.0567
$c_{+,0}$	1.8169	0.0453	1.0000	−0.3532	−0.6247	−0.4534	0.1671	−0.2710	0.2122	−0.2545	−0.3595
$c_{+,1}$	0.2803	0.2661	−0.3532	1.0000	−0.0280	−0.3974	−0.2226	0.7687	0.0216	−0.0133	−0.2866
$c_{+,2}$	−0.7542	0.0411	−0.6247	−0.0280	1.0000	−0.0035	0.2323	−0.0341	−0.3524	0.4313	0.0124
$c_{+,4}$	−0.0936	0.1461	−0.4534	−0.3974	−0.0035	1.0000	−0.2261	−0.2842	0.0044	−0.0123	0.7535
$c_{0,0}$	0.5310	0.0269	0.1671	−0.2226	0.2323	−0.2261	1.0000	−0.3095	−0.8652	0.8331	−0.2633
$c_{0,1}$	0.2273	0.1057	−0.2710	0.7687	−0.0341	−0.2842	−0.3095	1.0000	0.0950	−0.0942	−0.4221
$c_{0,2}$	0.2996	0.0748	0.2122	0.0216	−0.3524	0.0044	−0.8652	0.0950	1.0000	−0.9836	−0.0143
$c_{0,3}$	−0.0938	0.0590	−0.2545	−0.0133	0.4313	−0.0123	0.8331	−0.0942	−0.9836	1.0000	0.0069
$c_{0,4}$	−0.0136	0.0567	−0.3595	−0.2866	0.0124	0.7535	−0.2633	−0.4221	−0.0143	0.0069	1.0000

Following the same strategy as in Ref. [10], we introduce a set of reference q^2 values in the range where we have lattice data. By determining the form factors, their statistical uncertainty and all systematic uncertainties at these reference points, we obtain synthetic data points which include the complete and fully correlated error budget. These serve as inputs for the extrapolation over the entire kinematically allowed range $q^2 \in [0, q^2_{\mathrm{max}}]$.

We distinguish between different contributions to the full error budget. The statistical uncertainty is computed from the bootstrap analysis of the chiral and continuum extrapolation described in Sec. III C. We assess the systematic error arising from these fits in Sec. IV A by applying cuts to the data entering the fit as well as varying the functional description of the data, i.e., Eq. (27).

We estimate all remaining sources of uncertainty in Secs. IV B to IV H. Finally, in Sec. IV I, we address how to combine these various sources of uncertainty to complete the error budget.

A. Chiral-continuum extrapolation

We estimate the systematic uncertainty from the chiral-continuum extrapolation for $B_s \to K\ell\nu$ by performing cuts to the data as well as varying the fit ansatz in Eq. (27). We consider the following variations to the fit form:

(a) omitting the finite volume corrections (the second term in δf),
(b) omitting the term proportional to a^2 ($c_4 \equiv 0$),
(c) omitting the term proportional to M_π^2 ($c_1 \equiv 0$),
(d) analytic fits omitting the chiral logarithms ($\delta f \equiv 0$),

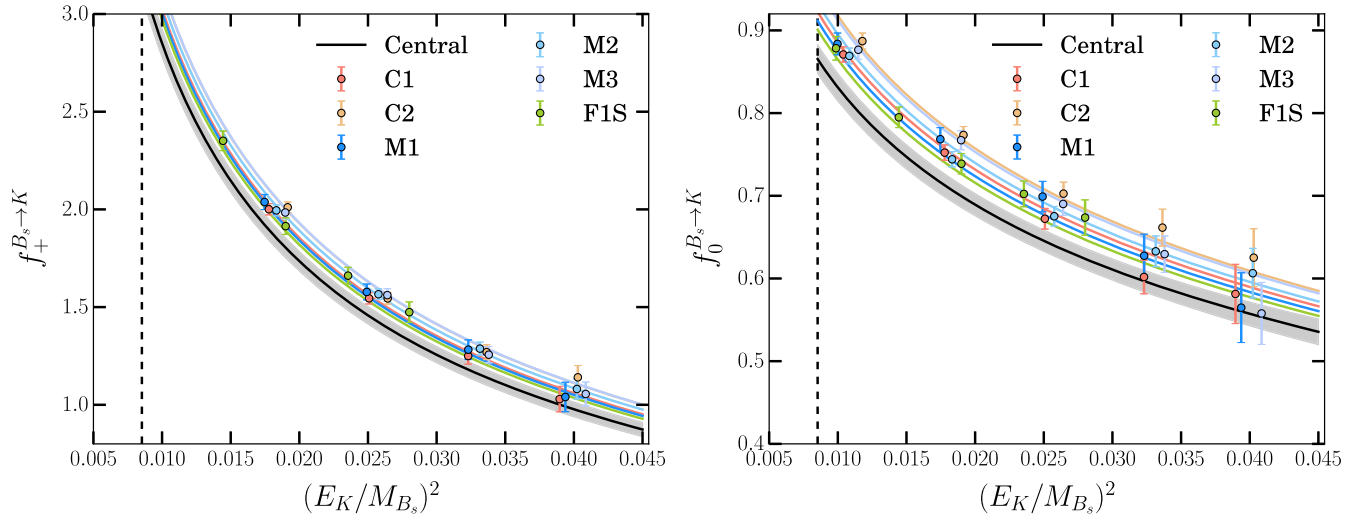

FIG. 4. Chiral-continuum extrapolation for the $B_s \to K\ell\nu$ form factors f_+ (left) and f_0 (right). The colored data points show the underlying data. The colored lines show the result of the fit evaluated at the parameters of the respective ensembles. The gray bands display the obtained form factors in the chiral-continuum limit and the associated statistical uncertainty.

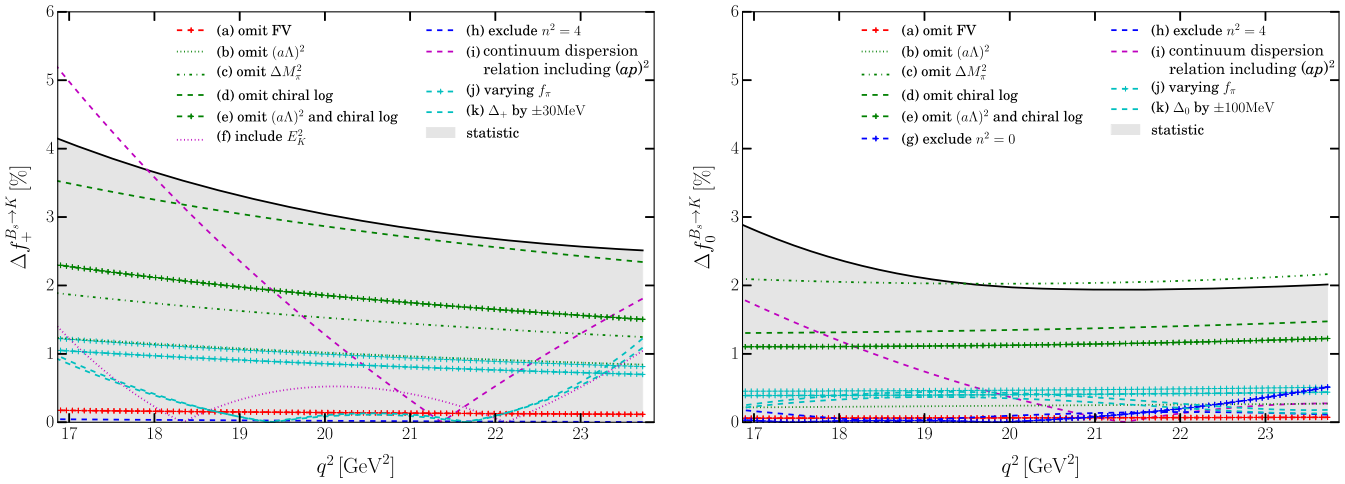

FIG. 5. Relative changes, $\Delta f_X = |f_X^{\text{pref}} - f_X^{\text{alt}}|/f_X^{\text{pref}}$ for $X = 0, +$, of the form-factor central values under variations of the chiral-continuum fit for $B_s \to K\ell\nu$. The shaded band shows the statistical uncertainty of the preferred fit.

(e) analytic fits simultaneously omitting the chiral logarithms and the a^2 term,
(f) including the term proportional to $(E_K/\Lambda)^2$ into the fit for f_+,

We also vary the data that enters the fit by:

(g) omitting the data points at the highest momentum, $\mathbf{p}_K = 2\pi(2,0,0)/L$ (smallest q^2),
(h) omitting the data points at zero momentum, i.e., q^2_{max} in f_0,
(i) using form factor data that have been obtained by imposing the continuum dispersion relation which at leading order differs from the lattice dispersion relation by powers $(ap)^2$. We therefore also include a term $c_{X,5}$ in these fits.

Finally, we consider the impact of variations of some of the numerical values of parameters entering the fit, such as:

(j) replacing the numerical value of f_π by its chiral limit value $f_0 = 112$ MeV [20] or by $f_K = 155.7$ MeV [15],
(k) varying the model estimate of $M_{B^*(0^+)}$ entering Δ_0 by ±100 MeV and the experimentally precisely known value of M_{B^*} entering Δ_+ by a generous ±30 MeV.

Figure 5 shows the relative effects of these variations compared to the statistical uncertainty of the central fit (gray shaded area). We notice that our fit is insensitive to most of these variations. The largest deviations are observed for variations including the lattice spacing and the pion-mass dependence, i.e., variations b, c, and d. However, even these remain of the same size as the statistical errors we quote. We take the largest difference between the preferred fit and any of the alternatives as the systematic uncertainty due to the chiral-continuum extrapolation.

An important subtlety is worth highlighting here. In previous work on the $B_s \to K\ell\nu$ semileptonic form factors [10,11], but also other decay channels like, e.g., $B \to \pi\ell\nu$ semileptonic [10,80], it was assumed that the pole locations of the *physical* form factors f_+ and f_0 also describe the kinematical behavior of $f_\perp$ and $f_\parallel$, respectively. In particular, based on the linear relations in Eqs. (4) and (5), $f_\perp$ was assumed to be dominated by f_+ and $f_\parallel$ by f_0. In Fig. 6, we compare the results when extrapolating the lattice data in both cases using Eq. (27). While with the current level of statistical precision no significant difference is observed for f_+, a significant difference—which increases with the kaon energy—can be observed for f_0. Since form-factor parametrizations often rely on the kinematical constraint $f_+(0) = f_0(0)$, this is a relevant problem for both the vector and scalar form factor. An interesting question in this context is whether this observation could explain the observed tensions between different sets of lattice results for $B_s \to K\ell\nu$, as

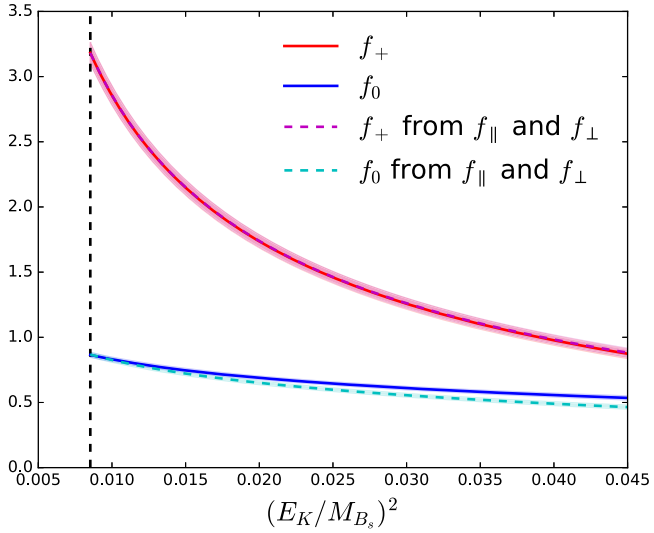

FIG. 6. The plot shows the result of the chiral-continuum fit based on Eq. (27), once using $f_\parallel$ and $f_\perp$ as input (and subsequently converted to f_0 and f_+) and once using f_0 and f_+ as input. The results for f_0 differ significantly and increasingly as the kaon momentum is increased.

observed by FLAG 21 [15]. Regarding the $B_s \to K\ell\nu$ decay, we note that HPQCD in Ref. [81] carried out the chiral and continuum limits based on the vector and scalar form factors. In line with our observation, their results for f_+ show a distinctly milder curvature as the results of Ref. [10,11] (cf. Fig. 32 in FLAG 21 [15]).

B. Lattice-scale uncertainty

We propagate the uncertainty of the lattice-scale determination (cf. Table I) by creating a Gaussian distribution with the correct central value and width, which is then used to convert the dimensionless lattice masses into dimensionful quantities prior to the chiral-continuum extrapolations. We therefore do not account separately for this uncertainty.

C. Strange-quark-mass uncertainties

1. Valence strange-quark-mass uncertainty

The $B_s \to K\ell\nu$ form factors depend explicitly on the valence-strange-quark mass, so the effects of any mistunings in this mass must be accounted for. In order to estimate the corresponding systematic uncertainty, we evaluate the form factors for additional choices of the spectator-quark mass on the C1 ensemble. We determine the fractional change of the form factor with respect to a percentage mistuning in the strange-quark mass; i.e., for $X = +, 0$ we compute

$$\Delta f_X/\Delta m_s \equiv \frac{f_X(am_s) - f_X(am_s^{\rm phys})}{am_s - am_s^{\rm phys}} \frac{am_s^{\rm phys}}{f_X(am_s^{\rm phys})}. \tag{29}$$

We repeat this for the different choices of momenta and take the largest value this ratio takes, which occurs at the smallest momentum. We tabulate the maximal values of this term for the form factors f_+ and f_0 in Table V. The largest deviation from the physical strange quark mass occurs on the F1S ensemble, where $am_s^{\rm sim} = 0.02144$ and $am_s^{\rm phys} = 0.02167(20)$. Allowing for one standard deviation, we find

$$\Delta m_s = \max\left\{\frac{|am_s^{\rm sim} - (am_s^{\rm phys} \pm \delta am_s^{\rm phys})|}{am_s^{\rm phys}}\right\} = 1.98\%. \tag{30}$$

TABLE V. Partial derivatives of the form factor as a function of the strange quark mistuning as defined in the text.

	$f_0^{B_s\to K}$	$f_+^{B_s\to K}$
$\Delta f_X/\Delta m_s$	0.0630(46)	0.1027(84)
$\max(\Delta m_s)[\%]$	1.98	1.98
$\max(\Delta f_X)[\%]$	0.13	0.20

Combining this with the above, we determine the maximal deviations as shown in the last line of Table V. We find that the largest impact of the strange quark mistuning is 0.20% for f_+ and 0.13% for f_0 which are far smaller than our leading uncertainties and therefore negligible.

2. Strange-sea-quark mistuning

Our fit functions do not depend explicitly on the strange sea-quark mass, and at each lattice spacing, we have form factors for only a single value of this mass. We estimate any systematic effects stemming from the sea strange-quark mistuning (which is largest on the coarse ensembles) in the same way, but including an additional suppression factor of α_s. Numerically, this is approximately $\Delta f_X/\Delta m_s \times \alpha_s \times \max(\Delta m_s^{\rm sea}) = 0.28\%$ and 0.46% for f_0 and f_+, respectively. This is intended as a conservative estimate for this uncertainty, and it is a negligible contribution to the total error budget.

D. Effects of the RHQ parameter uncertainty on the form factors

As outlined in Appendix A, the RHQ tuning procedure determines three coefficients in the RHQ action. These are the bare b-quark mass ($m_0 a$), the clover coefficient (c_P), and the anisotropy (ζ). The experimental inputs to this tuning are the measured B_s-meson mass and the hyperfine splitting ($\Delta M_{B_s} \equiv M_{B_s^*} - M_{B_s}$). In addition, the lattice scale and the physical strange-quark mass are required inputs. Furthermore, we enforce that the rest mass equals the kinetic mass. The tuned parameters, including estimates for all relevant sources of uncertainties, are listed in Table XVII in Appendix A.

In order to propagate the effect of these tuning uncertainties onto the form factors, we generated additional form factor data for different choices of the RHQ parameters on the C1 ensemble. Using this dataset, we determine the partial derivatives of the form factors with respect to the respective RHQ parameters. We normalize these values by the ratio of the tuned form factor and respective RHQ parameters on this ensemble and conservatively quote the maximum value this takes. These values are listed in the first two rows of Table VI.

We derive the uncertainty on the form factor due to a given RHQ parameter by multiplying these normalized derivatives on the C1 ensemble with the relative uncertainty of this RHQ parameter on a given lattice spacing. We illustrate this on the example of ζ,

$$\left(\frac{\delta f_X}{f_X^{\rm tuned}}\right)_\zeta = \max_{\mathbf{n}}\left(\frac{\zeta^{\rm tuned}}{f_X^{\rm tuned}}\frac{\partial f_X}{\partial \zeta}\right)\Big|_{C1} \frac{\delta\zeta}{\zeta^{\rm tuned}}, \tag{31}$$

where $f_X^{\rm tuned}$ is the form factor evaluated at the tuned value of the RHQ parameters on C1, while the last term is evaluated lattice spacing by lattice spacing.

TABLE VI. Estimates for the normalized partial derivatives on the C1 ensemble (top two rows) and the maximum uncertainty propagated onto the form factors.

	am_0	ζ	c_P
f_+ max normalized slope	0.2368	0.1003	0.0543
f_0 max normalized slope	0.1067	0.0418	0.1089
f_+ RHQ uncertainty [%]	0.8145	0.9004	0.3215
f_0 RHQ uncertainty [%]	0.3670	0.3755	0.6448

We find that the uncertainty is largest on the F1S ensemble and therefore take this to provide a conservative estimate for the RHQ parameter tuning on the form factors and list their values in the last two rows of Table VI. Adding these contributions in quadrature, we quote an uncertainty of 1.26% on f_+ and 0.83% on f_0.

E. Discretization errors

Due to their different origin and size, we separately discuss discretization errors due to the light quarks and gluons in the action, the heavy-light current, and the RHQ quarks.

1. Discretization effects from the action and the current

The dominant discretization error from the light quarks and gluons in the action is $O((a\Lambda_{\rm QCD})^2)$ which, using $\Lambda_{\rm QCD} = 500$ MeV, amounts to ∼3.2% on the finest ensemble. This is accounted for by including a^2-terms in the chiral-continuum extrapolations. We assign the estimate $(a\Lambda_{\rm QCD})^4 \sim 0.10\%$ for subsequent terms. Potential uncertainties stemming from the residual chiral symmetry breaking are estimated to be of the size $am_{\rm res} \sim 0.1\%$ for the light quarks.

The leading quark and gluon discretization errors in the heavy-light currents are $O(\alpha_s a\tilde{m}_l, (a\tilde{m}_l)^2, \alpha_s^2 a\Lambda_{\rm QCD}, (ap)^2)$.

In the comparison between our central fit and the variations (i) and (g), we do not observe any evidence of sizable momentum-dependent discretization errors in our data. Thus, we do not include a systematic error from this source.

Estimating the effects by power counting on the fine ensemble, the first two terms are negligible (<0.1%), while the third amounts to ∼0.78%. Combining this in quadrature with the $(a\Lambda_{\rm QCD})^4$ and $am_{\rm res}$ from above, we quote 0.79%.

2. Heavy quark discretization errors

The RHQ action gives rise to nontrivial lattice-spacing dependence in the form factors when $m_0 a \sim 1$. To estimate the resulting discretization errors, we use the same power-counting approach as in our previous papers [10,33,38]. For reproducibility and completeness, we provide a brief summary of the procedure as well as intermediate numerical values in Appendix B. We take the size of heavy-quark discretization errors in our calculation of semileptonic form factors from the estimate on our finest ensemble ($a^{-1} = 2.785$ GeV). They amount to ∼1.3% for the lattice form factor $f_\parallel$ and ∼1.5% for $f_\perp$.

F. Renormalization factor

The renormalization factor relating the lattice weak current to the continuum one is shown in Eq. (8) in Sec. II C, where $Z^{bl}_{V_\mu}$ is given by a product of three components. We consider the uncertainties from these three multiplicative factors separately and add them in quadrature to obtain the total error on the form factors.

For Z^{ll}_V, we use the nonperturbatively determined value of the axial-current renormalization factor Z_A evaluated at the value of the light quark mass (see Table II for numerical values). We can neglect the statistical uncertainty in Z_A (which is only 0.02% on the finer ensembles) and the difference between Z^{ll}_V and Z_A [which is $O(am_{\rm res}) \sim 7 \times 10^{-4}$ at $a \approx 0.086$ fm].

For Z^{bb}_V, we use the nonperturbative determination from Ref. [38]. The statistical uncertainty in Z^{bb}_V on the finer ensemble is well below 1% and propagated into the statistical error analysis. The perturbative truncation error in ρ^{bl}_V is taken to be the full size of the one-loop correction at the finer $a \approx 0.086$ fm lattice spacing, which leads to 1.7% for ρ_{V_0} and 0.6% for ρ_{V_i}. We use the values of ρ_{V_μ} and Z^{ll}_V in the chiral limit and must consider errors due to the nonzero physical up, down, and strange masses. The leading quark-mass dependent errors in ρ_{V_μ} and Z^{ll}_V are $O(\alpha_s a\tilde{m}_q)$ and $O((a\tilde{m}_q)^2)$, respectively, but these are already accounted for in our estimate of light-quark and gluon discretization errors (see Sec. IV E 1), and we do not count them again here.

Perturbative truncation errors are by far the dominant source of uncertainty in the renormalization factor, and the quadrature sum of the three error contributions is 1.7% for $f_\parallel$ and 0.6% for $f_\perp$.

G. Finite-volume corrections

As discussed in Sec. III C, we directly account for the finite size effects in the chiral continuum extrapolation [i.e., in Eq. (27)]. We can assess the numerical size of these effects by comparing to a fit that does not include the second term in Eq. (28). The maximum deviation for f_0 (f_+) is given by 0.06% (0.13%).

H. Isospin breaking

The leading quark-mass contribution to the isospin breaking from the valence-quark masses is of $O((m_d - m_u)/\Lambda_{\rm QCD}) \sim 0.5\%$, obtained using $m_d - m_u = 2.38(18)$MeV [82] and $\Lambda_{\rm QCD} = 500$ MeV. The difference between the u and d-quark masses in the sea sector should have a negligible

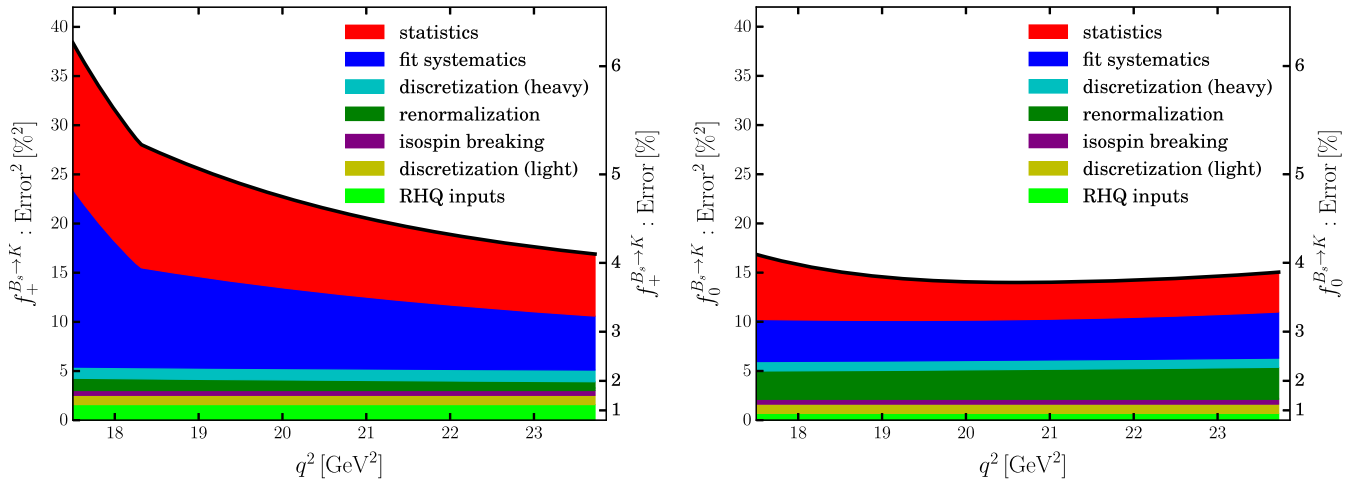

FIG. 7. Cumulative systematic errors for the chiral- and continuum-extrapolated form factor for $B_s \to K\ell\nu$.

effect on the form factors because the sea quarks couple to the valence quarks through $I = 0$ gluon exchange, giving an uncertainty of $O(((m_d - m_u)/\Lambda_{\rm QCD})^2) \sim 0.003\%$. The electromagnetic contribution to isospin breaking is expected to be $O(\alpha_{\rm QED}) \sim 1/137 = 0.7\%$. We therefore take 0.7% as the uncertainty from isospin breaking and electromagnetic effects.

I. Form factor results and correlation matrices

In the next section, we will fit a z-expansion to synthetic data for the physical form factors in the continuum and infinite-volume limit, generated at selected values of q^2, to extend our form factors to the full kinematic range. Because we first extrapolate to the continuum limit and then perform the z-expansion to extend the form factors over the full kinematic range, the number of available independent reference q^2 values is restricted by the number of resolved parameters in the chiral-continuum limit of the HMχPT description of the lattice data. Since we resolve 3 (2) parameters that parametrize the continuum form factors f_0 (f_+), the number of synthetic data points we can choose is limited by this. We account for the correlations between the form factors at these q^2 values as follows.

The total error budget can be divided into three major contributions: the statistical uncertainty, the uncertainties associated to the chiral-continuum extrapolation, and the uncertainties that are estimated as a constant q^2 independent percentage of the form factors. We refer to these as statistical, fit systematic, and flat systematic. While most of the latter are estimated as a percentage uncertainty on the form factors f_+ and f_0, the contributions described in Secs. IV E 2 and IV F are determined with respect to the form factors $f_\parallel$ and $f_\perp$, which induces a mild q^2 dependence when this is related to f_+ and f_0. The resulting cumulative systematic errors for $B_s \to K\ell\nu$ are illustrated in Fig. 7. We now provide more detail on estimating the correlations of the different sources of uncertainties at the reference values.

It is straightforward to obtain the statistical correlations from the bootstrap analysis of the chiral and continuum fit in Sec. III C.

The systematic error for the chiral-continuum extrapolation is found by varying the fit function and parametric inputs, as described above. This does not provide information on correlations between different q^2-values. However, alternate chiral-continuum fits with different fit functions exhibit very similar statistical correlations between q^2-bins. Hence, we take the statistical correlation matrix from our preferred fit and multiply it by the estimated chiral-continuum extrapolation error at each q^2 value. For off-diagonal elements of the correlation matrix, we use the product $\sigma_{q_i^2}\sigma_{q_j^2}$.

We assume each of the remaining "flat" systematic errors to be 100% correlated and add the corresponding covariance matrices. Where the percent error is given for $f_\parallel$ and $f_\perp$, we first construct the corresponding covariance matrix for $f_\parallel$ and $f_\perp$ and then propagate the correlated error in order to obtain the covariance matrix for f_+ and f_0. Table VIII shows the resulting statistical and systematic correlation matrices, which enable the full reconstruction of the total covariance matrices using the form factor values and errors from Table VII.

V. PHENOMENOLOGICAL APPLICATIONS

A. z-expansions of form factors

Once we have continuum values for the form factors, we extrapolate them over the entire physical range of q^2 using a fit to a z-expansion [83–90]. The squared momentum transfer, q^2, is mapped to the variable z using

$$z(q^2; t_*, t_0) = \frac{\sqrt{t_* - q^2} - \sqrt{t_* - t_0}}{\sqrt{t_* - q^2} + \sqrt{t_* - t_0}}. \tag{32}$$

TABLE VII. Values and error budgets for the $B_s \to K\ell\nu$ form factors at three representative q^2 values in the range of simulated lattice momenta. The total error is obtained by adding the individual errors in quadrature. See Table VIII for the corresponding correlation matrices. The data shown in this table are contained in the accompanying data file.

	f_+		f_0		
q^2 [GeV^2]	17.60	23.40	17.60	20.80	23.40
$f_{+,0}(q^2)$	0.9878	2.9301	0.5594	0.6843	0.8397
	Error budget (absolute contribution)				
Statistical error	0.0377	0.0743	0.0141	0.0133	0.0167
Chiral-continuum extrapolation	0.0407	0.0698	0.0116	0.0139	0.0180
Other	0.0240	0.0700	0.0139	0.0172	0.0213
Total	0.0604	0.1236	0.0230	0.0258	0.0325
	Error budget (in per cent)				
Statistical error	3.82	2.54	2.53	1.94	1.99
Chiral-continuum extrapolation	4.12	2.38	2.06	2.03	2.14
Other	2.43	2.39	2.49	2.51	2.54
Total	6.12	4.22	4.10	3.77	3.87

This transformation maps the complex q^2 plane, with a cut for $q^2 \geq t_*$, onto the unit disk in z. For use below, we set $t_\pm = (M_{B_s} \pm M_K)^2$, with $t_- = q^2_{\rm max}$, while t_* is fixed by the appropriate two-particle production threshold $t_* = (M_B + M_\pi)^2$. The value of t_0 can be chosen to fix the range in z corresponding to a given range in q^2. We choose

$$t_0 = t_{\rm opt} = t_* - \sqrt{t_*(t_* - t_-)}. \tag{33}$$

This symmetrizes the range of z about zero for $0 \leq q^2 \leq q^2_{\rm max}$, which is mapped onto the real axis $0.2 \gtrsim z \gtrsim -0.2$, indicating that an expansion of the form factor in z rather than in q^2 might converge quickly. This motivated Boyd, Grinstein, and Lebed (BGL) [84] to write the form factor as

$$f_X(q^2) = \frac{1}{B_X(q^2)\phi_X(q^2, t_0)} \sum_{n\geq 0} a_{X,n}(t_0) z^n, \tag{34}$$

where $\phi_X(q^2, t_0)$ is known as the outer function, with expressions given in Appendix D. For $X = +, 0$, the Blaschke factor $B_X(q^2)$ is chosen to vanish at the positions of subthreshold poles M_i^X,

$$B_X(q^2) = \prod_{i \in X{\rm poles}} z(q^2; t_*, (M_i^X)^2). \tag{35}$$

For f_+, the measured 1^- vector-meson with $M^+_{B^*(1^-)} = 5.32471$ GeV [50] sits above the physical semileptonic region $0 \leq q^2 \leq q^2_{\rm max}$, but also below the $B\pi$ threshold. Specifically, $q^2_{\rm max} \leq (M^+_{B^*(1^-)})^2 \leq t_* \to 23.73\ {\rm GeV}^2 \leq 28.35\ {\rm GeV}^2 \leq 29.35\ {\rm GeV}^2$. We cancel this pole through the corresponding Blaschke factor $B_+(q^2)$ prior to expanding in z. For f_0, the theoretically predicted pole mass $M^0_{B^*(0^+)} = 5.63$ GeV [51] sits above the $B\pi$ threshold, and no pole needs to be canceled.

The following unitarity constraint applies,

$$\frac{1}{2\pi i} \oint_C \frac{dz}{z} \theta_z |B_X(q^2)\phi_X(q^2, t_0) f_X(q^2)|^2 \leq 1, \tag{36}$$

with C the unit circle, $\theta_z \equiv \theta(\alpha_{B_sK} - |\arg[z]|)$ and $\alpha_{B_sK} = \arg[z(t_+, t_*, t_0)]$. Since for the $B_s \to K\ell\nu$ transition the two-particle $B\pi$ production threshold lies below the B_sK threshold, i.e., $t_* < t_+$, the unitarity constraint originally proposed by BGL [84] needs to be modified. This is similar to the situation discussed in Refs. [91–94], but note some differences in notation in those papers, in particular our use of t_* and t_+ for the locations of the $B\pi$ and B_sK production thresholds, respectively. The step function θ_z achieves this by restricting the integration over the unit circle to the relevant arc. Let us now define the inner product

$$\begin{aligned} \langle z^i | z^j \rangle_\alpha &= \frac{1}{2\pi} \int_{-\alpha}^{\alpha} d\phi (z^i)^* z^j \Big|_{z=e^{i\phi}}, \\ &= \begin{cases} \frac{\sin(\alpha(i-j))}{\pi(i-j)} & i \neq j \\ \frac{\alpha}{\pi} & i = j \end{cases} \end{aligned} \tag{37}$$

on the arc $[-\alpha, +\alpha]$ of the unit circle. When the inner product is defined over the entire unit circle, $[-\pi, +\pi]$, the monomials z^i are orthonormal, $\langle z^i | z^j \rangle_\pi = \delta_{ij}$. In that case, the unitarity constraint (36) becomes $\sum_i |a_{X,i}|^2 \leq 1$. With the restriction to the arc $[-\alpha_{B_sK}, +\alpha_{B_sK}]$, the modified BGL unitarity constraint developed in Ref. [95] is

TABLE VIII. Statistical, fit- and flat-systematic errors $\delta f_{+/0}$ for representative q^2 values (given in units of GeV^2 as arguments of $f_{+/0}$), and corresponding correlation matrices. The data shown in this table are contained in the accompanying data file.

			f_+		f_0		
			17.60	23.40	17.60	20.80	23.40
	q^2 [GeV^2]	$\delta f_{+/0}$	0.0377	0.0743	0.0141	0.0133	0.0167
f_+	17.60	0.0377	1.0000	0.8254	0.6976	0.7540	0.7212
	23.40	0.0743	0.8254	1.0000	0.5165	0.7632	0.8008
f_0	17.60	0.0141	0.6976	0.5165	1.0000	0.8118	0.7117
	20.80	0.0133	0.7540	0.7632	0.8118	1.0000	0.9699
	23.40	0.0167	0.7212	0.8008	0.7117	0.9699	1.0000

Statistical

			f_+		f_0		
			17.60	23.40	17.60	20.80	23.40
	q^2 [GeV^2]	$\delta f_{+/0}$	0.0407	0.0698	0.0116	0.0139	0.0180
f_+	17.60	0.0407	1.0000	0.8254	0.6976	0.7540	0.7212
	23.40	0.0698	0.8254	1.0000	0.5165	0.7632	0.8008
f_0	17.60	0.0116	0.6976	0.5165	1.0000	0.8118	0.7117
	20.80	0.0139	0.7540	0.7632	0.8118	1.0000	0.9699
	23.40	0.0180	0.7212	0.8008	0.7117	0.9699	1.0000

Fit systematic

			f_+		f_0		
			17.60	23.40	17.60	20.80	23.40
	q^2 [GeV^2]	$\delta f_{+/0}$	0.0240	0.0700	0.0139	0.0172	0.0213
f_+	17.60	0.0240	1.0000	0.9974	0.9461	0.9419	0.9368
	23.40	0.0700	0.9974	1.0000	0.9229	0.9178	0.9115
f_0	17.60	0.0139	0.9461	0.9229	1.0000	0.9999	0.9995
	20.80	0.0172	0.9419	0.9178	0.9999	1.0000	0.9998
	23.40	0.0213	0.9368	0.9115	0.9995	0.9998	1.0000

Flat systematic

$$\sum_{i,j\geq 0} a^*_{X,i}\langle z^i|z^j\rangle_{\alpha_{B_sK}} a_{X,j} \equiv |\mathbf{a}_X|^2_{\alpha_{B_sK}} \leq 1, \tag{38}$$

where we have defined $|\mathbf{a}_X|^2_{\alpha_{B_sK}}$ to mean the quadratic form on the left-hand side.

B. Extrapolation to $q^2 = 0$

To extrapolate our results to the full physical range of q^2, we start from the results for f_+ and f_0 listed in Table VII, with statistical and systematic errors and correlations given in Table VIII, added in quadrature. Input parameters for the z fits are summarized in Table IX. We use the short-hand vector notation $\mathbf{f} = (\mathbf{f}_+, \mathbf{f}_0)^T$ for the vector and scalar form factors at the kinematical reference points and denote the corresponding covariance matrix by $C_\mathbf{f}$. We fit the data to a z-parametrization of Eq. (34), subject to the unitarity constraint (38) and the kinematical constraint $f_+(0) = f_0(0)$.

In the Bayesian-inference strategy for fitting form factors developed in Ref. [95], the unitarity constraint is implemented as a flat prior, which acts as a regulator for the fitting problem. In contrast to frequentist fits, this allows us to determine the parameters of a BGL parametrization to arbitrarily high order, removing errors from truncating the power series in z in Eq. (34).

The Bayesian-inference problem of determining the BGL parameters $\mathbf{a} = (\mathbf{a}_+, \mathbf{a}_0)^T$ and functions $g(\mathbf{a})$ of them amounts to computing expectation values

$$\langle g(\mathbf{a})\rangle = \mathcal{N}\int d\mathbf{a} g(\mathbf{a})\pi(\mathbf{a}|\mathbf{f}, C_\mathbf{f})\pi_\mathbf{a}, \tag{39}$$

TABLE IX. Input masses for the BGL z fits. Values are in GeV [50]. The superscript † indicates, where the isospin-averaged mass has been taken.

M_B	M_{B_s}	M_π	M_K	$M^+_{B^*(0^+)}$
5.27950†	5.36682	0.138039†	0.495644†	5.32471

where $\mathcal{N}$ is a normalization constant. As prior knowledge on the form factor, we use only the unitarity constraint expressed in terms of the distribution

$$\pi_{\mathbf{a}} \propto \theta(1 - |\mathbf{a}_+|^2_{\alpha_{B_sK}})\theta(1 - |\mathbf{a}_0|^2_{\alpha_{B_sK}}), \tag{40}$$

which essentially limits the integration range in Eq. (39). The conditional probability density for the parameter $\mathbf{a}$ given the fit model and data is

$$\pi(\mathbf{a}|\mathbf{f}, C_\mathbf{f}) \propto \exp\left(-\frac{1}{2}\chi^2(\mathbf{a}, \mathbf{f})\right), \tag{41}$$

where

$$\chi^2(\mathbf{a}, \mathbf{f}) = (\mathbf{f} - Z\mathbf{a})^T C_\mathbf{f}^{-1}(\mathbf{f} - Z\mathbf{a}). \tag{42}$$

Following Ref. [95], the matrix Z consists of diagonal blocks

$$(Z_{XX})_{ij} = \frac{z^j}{B_X(q_i^2)\phi_X(q_i^2, t_0)}, \tag{43}$$

where XX is either $++$ or 00, for the vector or scalar form factors, respectively. The off-diagonal blocks, which implement the kinematical constraint $f_+(0) = f_0(0)$, are

$$(Z_{+0})_{ij} = 0,$$
$$(Z_{0+})_{ij} = \frac{1}{z(0; t_*, M_{B^*}^2)\phi_+(0)}\frac{\phi_0(0)}{\phi_0(q_i^2)} z^j(0). \tag{44}$$

The integral in Eq. (39) can be performed by Monte Carlo, which corresponds to drawing multivariate normal-distributed pseudorandom numbers. An efficient algorithm and an implementation in PYTHON are presented in Refs. [95,96]. The results presented here are based on 2000 samples.

Figure 8 shows the results of z-fits to our $B_s \to K\ell\nu$ data, with numerical values for the fit parameters in Table X.

For the discussion of the results, it is also worthwhile, in parallel, to have a look at the first data column of Table XI, which shows the result for the form factor extrapolated to $q^2 = 0$. For both the coefficients $\mathbf{a}$ and $f_+(0)$, we find significant variation in both error and central value when increasing the order of the z expansion from $K_{+,0} = 2$. We find stable central values and errors for $K \geq 3$. Higher-order coefficients can be added to the fit (the tables show results up to $K_{+,0} = 10$), whereby the errors on the significantly determined lower-order coefficients and also the result for $f_{+,0}(0)$ remain stable, and the higher-order coefficients are compatible with zero. We conclude that the form factor parametrization determined in this way becomes truncation independent for large-enough $K_{+,0}$. For the following analyses, we use results with $(K_+, K_0) = (5, 5)$.

Furthermore, the value of the form factors at $q^2 = 0$ is of interest for comparison with predictions from different theoretical methods. Using light cone sum rules, Duplancic and Melic report $f(0) = 0.30(^{+4}_{-3})$ [97], and Khodjamirian and Rusov quote $f(0) = 0.336(23)$ [98]. Based on a relativistic quark model, Faustov and Galkin predict

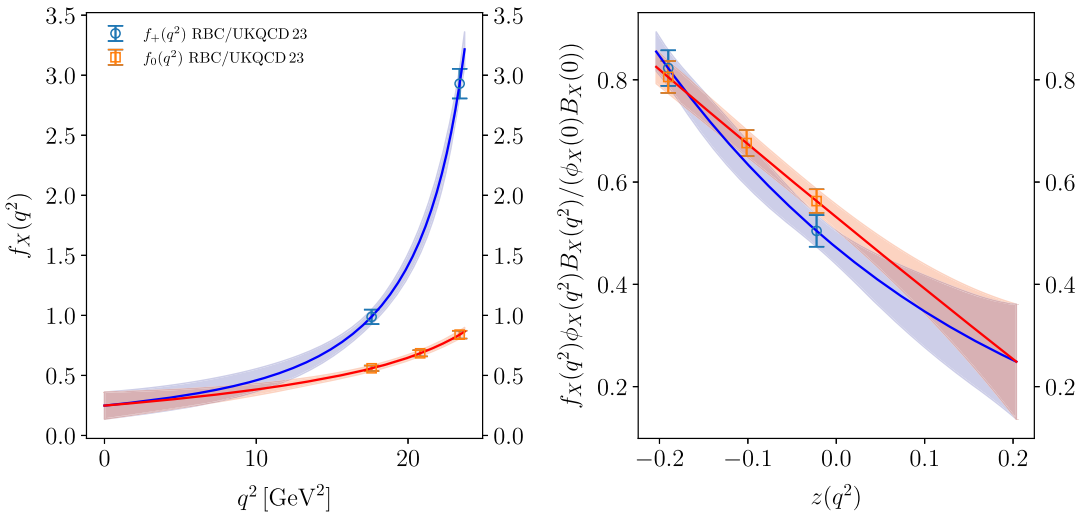

FIG. 8. z-fits to $B_s \to K\ell\nu$ form factors for $(K_+, K_0) = (5, 5)$, plotted against q^2 (left) and against z (right), where in the latter plot the outer function and Blaschke factor has been removed. Blue denotes f_+, and red denotes f_0.

TABLE X. Results for z-fits to data for scalar and vector form factors for $B_s \to K\ell\nu$. The main results of this paper are the ones with $(K_+, K_0) = (5,5)$. The data for this case and the corresponding correlation matrix is contained in the accompanying data file.

K_+	K_0	$a_{+,0}$	$a_{+,1}$	$a_{+,2}$	$a_{+,3}$	$a_{+,4}$	$a_{+,5}$	$a_{+,6}$	$a_{+,7}$	$a_{+,8}$	$a_{+,9}$
2	2	0.0293(11)	−0.0871(46)	⋯	⋯	⋯	⋯	⋯	⋯	⋯	⋯
2	3	0.0249(16)	−0.0999(57)	⋯	⋯	⋯	⋯	⋯	⋯	⋯	⋯
3	2	0.0245(16)	−0.0799(50)	0.093(21)	⋯	⋯	⋯	⋯	⋯	⋯	⋯
3	3	0.0245(15)	−0.078(12)	0.101(49)	⋯	⋯	⋯	⋯	⋯	⋯	⋯
3	4	0.0246(16)	−0.078(16)	0.100(70)	⋯	⋯	⋯	⋯	⋯	⋯	⋯
4	3	0.0246(17)	−0.075(31)	0.102(49)	−0.07(72)	⋯	⋯	⋯	⋯	⋯	⋯
4	4	0.0246(17)	−0.077(32)	0.100(68)	−0.03(70)	⋯	⋯	⋯	⋯	⋯	⋯
5	5	0.0246(17)	−0.074(31)	0.099(70)	−0.08(67)	0.05(70)	⋯	⋯	⋯	⋯	⋯
6	6	0.0247(16)	−0.073(32)	0.101(69)	−0.10(69)	0.09(74)	−0.05(71)	⋯	⋯	⋯	⋯
7	7	0.0247(17)	−0.071(33)	0.107(70)	−0.11(72)	0.08(89)	−0.04(89)	0.03(73)	⋯	⋯	⋯
8	8	0.0248(17)	−0.068(35)	0.102(74)	−0.18(77)	0.2(1.1)	−0.2(1.3)	0.1(1.2)	−0.06(82)	⋯	⋯
9	9	0.0248(18)	−0.068(38)	0.107(85)	−0.16(82)	0.2(1.4)	−0.2(1.9)	0.1(1.9)	−0.1(1.5)	0.03(89)	⋯
10	10	0.0247(18)	−0.067(43)	0.112(95)	−0.15(90)	0.2(1.8)	−0.2(2.6)	0.1(2.9)	−0.1(2.7)	−0.0(1.9)	0.02(98)

K_+	K_0	$a_{0,0}$	$a_{0,1}$	$a_{0,2}$	$a_{0,3}$	$a_{0,4}$	$a_{0,5}$	$a_{0,6}$	$a_{0,7}$	$a_{0,8}$	$a_{0,9}$
2	2	0.0981(36)	−0.286(14)	⋯	⋯	⋯	⋯	⋯	⋯	⋯	⋯
2	3	0.0917(39)	−0.331(19)	−0.211(53)	⋯	⋯	⋯	⋯	⋯	⋯	⋯
3	2	0.0950(37)	−0.263(15)	⋯	⋯	⋯	⋯	⋯	⋯	⋯	⋯
3	3	0.0953(43)	−0.254(41)	0.02(13)	⋯	⋯	⋯	⋯	⋯	⋯	⋯
3	4	0.0955(44)	−0.254(42)	0.02(22)	−0.02(60)	⋯	⋯	⋯	⋯	⋯	⋯
4	3	0.0954(43)	−0.254(40)	0.03(12)	⋯	⋯	⋯	⋯	⋯	⋯	⋯
4	4	0.0953(42)	−0.254(42)	0.02(21)	−0.02(60)	⋯	⋯	⋯	⋯	⋯	⋯
5	5	0.0954(44)	−0.254(41)	0.02(21)	−0.01(55)	−0.00(62)	⋯	⋯	⋯	⋯	⋯
6	6	0.0957(42)	−0.251(41)	0.04(21)	−0.01(52)	−0.06(65)	0.07(65)	⋯	⋯	⋯	⋯
7	7	0.0955(44)	−0.250(40)	0.06(20)	0.05(50)	−0.13(72)	0.17(79)	−0.12(69)	⋯	⋯	⋯
8	8	0.0954(43)	−0.250(41)	0.06(22)	0.06(50)	−0.18(84)	0.2(1.0)	−0.21(99)	0.10(74)	⋯	⋯
9	9	0.0956(44)	−0.247(41)	0.08(23)	0.06(50)	−0.27(96)	0.4(1.4)	−0.4(1.5)	0.3(1.2)	−0.15(80)	⋯
10	10	0.0956(42)	−0.245(42)	0.11(24)	0.11(49)	−0.4(1.1)	0.7(1.8)	−0.8(2.2)	0.7(2.1)	−0.4(1.5)	0.16(87)

$f(0) = 0.284(14)$ [99], where the NLO perturbative-QCD result by Wang and Xiao is $f(0) = 0.26(^{+4}_{-3})(2)$ [100]. All these values are compatible with our $(K_+, K_0) = (5,5)$ result

$$f(q^2 = 0) = 0.25(11); \tag{45}$$

however, our uncertainty at $q^2 = 0$ is substantially larger than for these other predictions.

TABLE XI. Results for observables based on the results for the z fits in Table X. The main results of this paper are the ones with $(K_+, K_0) = (5,5)$.

K_+	K_0	$f(q^2=0)$	$R^{\text{impr}}_{B_s\to K}$	$R_{B_s\to K}$	$\frac{\Gamma^\tau}{\lvert V_{ub}\rvert^2}$ $(\frac{1}{\text{ps}})$	$\frac{\Gamma^\mu}{\lvert V_{ub}\rvert^2}$ $(\frac{1}{\text{ps}})$	$V^{\text{low}}_{\text{CKM}}$	$V^{\text{high}}_{\text{CKM}}$	$V^{\text{full}}_{\text{CKM}}$
2	2	0.222(21)	1.545(17)	0.741(19)	5.37(43)	7.25(70)	0.00356(39)	0.00325(30)	0.00336(32)
2	3	0.087(39)	1.657(46)	0.954(75)	3.70(50)	3.94(81)	0.0070(22)	0.00408(46)	0.00420(52)
3	2	0.231(21)	1.721(57)	0.774(27)	4.34(45)	5.62(72)	0.00375(42)	0.00382(41)	0.00379(39)
3	3	0.248(88)	1.721(56)	0.76(10)	4.48(72)	6.1(1.7)	0.0039(14)	0.00381(46)	0.00381(52)
3	4	0.25(12)	1.722(64)	0.77(15)	4.51(84)	6.2(2.3)	0.0042(22)	0.00380(48)	0.00382(53)
4	3	0.249(86)	1.72(12)	0.76(12)	4.55(82)	6.3(2.0)	0.0039(16)	0.00378(53)	0.00379(59)
4	4	0.25(12)	1.72(12)	0.78(17)	4.53(89)	6.3(2.4)	0.0043(29)	0.00381(57)	0.00383(62)
5	5	0.25(11)	1.72(11)	0.77(16)	4.57(90)	6.4(2.4)	0.0041(24)	0.00376(55)	0.00378(61)
6	6	0.26(11)	1.71(11)	0.76(16)	4.63(88)	6.5(2.4)	0.0040(26)	0.00375(54)	0.00376(58)
7	7	0.26(11)	1.71(11)	0.75(15)	4.67(90)	6.7(2.4)	0.0038(19)	0.00373(56)	0.00374(62)
8	8	0.26(11)	1.70(12)	0.74(15)	4.71(94)	6.8(2.6)	0.0038(19)	0.00371(55)	0.00372(62)
9	9	0.27(11)	1.70(12)	0.74(16)	4.76(98)	7.0(2.7)	0.0038(20)	0.00370(59)	0.00371(66)
10	10	0.28(11)	1.71(13)	0.73(16)	4.80(99)	7.1(2.8)	0.0037(31)	0.00368(58)	0.00368(62)

C. Standard Model predictions

With the parametrization of the form factors $f_+(q^2)$ and $f_0(q^2)$ over the entire physical phase space $0 \le q^2 \le q^2_{\rm max}$ at hand, we consider a variety of phenomenological applications.

1. Determination of $|V_{ub}|$

The CKM matrix element $|V_{ub}|$ can be computed by comparing the differential decay rate in Eq. (1) to experimental data for the same exclusive decay. In practice, one compares the differential decay rate after integrating over q^2 bins. To date, only data for the branching fraction

$$R_{\rm BF} = \frac{\mathcal{B}(B_s^0 \to K^-\mu^+\nu_\mu)}{\mathcal{B}(B_s^0 \to D_s^-\mu^+\nu_\mu)} \tag{46}$$

for two q^2 bins from LHCb is available [16]. In particular, for the low ($q^2 \le 7$ GeV^2), high ($q^2 \ge 7$ GeV^2), and combined bins, we use

$$\begin{aligned} R_{BF}^{\rm low} &= 1.66(08)(09) \times 10^{-3}, \\ R_{BF}^{\rm high} &= 3.25(21)(^{+18}_{-19}) \times 10^{-3}, \\ R_{BF}^{\rm total} &= 4.89(21)(^{+24}_{-25}) \times 10^{-3}, \end{aligned} \tag{47}$$

where the first error is statistical and the second error the combined systematic uncertainty. $|V_{ub}|$ can still be determined by combining these results with the branching ratio [101]

$$\mathcal{B}(B_s^0 \to D_s^-\mu^+\nu_\mu) = 2.49(12)(21) \times 10^{-2}, \tag{48}$$

and the B_s^0 lifetime $\tau_{B_s^0} = 1.520(5) \times 10^{-12}$ s [50,102],

$$|V_{ub}| = \sqrt{\frac{R_{BF}^{\rm bin}\mathcal{B}(B_s^0 \to D_s^-\mu^+\nu_\mu)}{\tau_{B_s^0}\Gamma_0^{\rm bin}(B_s \to K\ell\nu)}}, \tag{49}$$

where bin is either "low" or "high." The reduced decay rate $\Gamma_0^{\rm bin} = \Gamma^{\rm bin}/|V_{ub}|^2$ is obtained from the lattice computation and integrated over the range of the experimental bin. We symmetrize errors and generate a multivariate distribution for the branching fractions and the lifetime, assuming no statistical correlation but the systematic errors to be 100% correlated (as, e.g., in Ref. [103]). In this way, we compute results for $|V_{ub}|$ for both bins individually and combined in terms of a weighted average taking into account correlations. We present our results in Table XI. Our final result, the one for $(K_+, K_0) = (5, 5)$, is

$$|V_{ub}| = 3.78(61) \times 10^{-3}, \tag{50}$$

and we emphasize that our predictions for the low and high q^2-bin are consistent within uncertainties. Repeating the analysis with vanishing experimental error, the result would be $|V_{ub}| = 3.73(37) \times 10^{-3}$, indicating that at this stage the error on the result in Eq. (50) is dominated by the experimental uncertainty. For comparison and used in the following section, we quote the results for $|V_{ub}|$ from the exclusive and inclusive analyses

$$|V_{ub}|^{\rm FLAG\,21}_{\rm exclusive} = 3.74(17) \times 10^{-3}\ [10, 15, 80, 104\text{–}107] \tag{51}$$

$$|V_{ub}|^{\rm PDG\,22}_{\rm inclusive} = 4.13(26) \times 10^{-3}\ [50, 102, 108\text{–}110]. \tag{52}$$

These two results are compatible within less than 2σ. Our result is compatible with both values, albeit with a larger overall error.

2. Differential decay width

The information provided by the analysis of our lattice data allows us to predict the shape of the differential decay width $d\Gamma/dq^2$ in the SM. Our results are shown in Fig. 9, assuming our result for $|V_{ub}|$ from Eq. (50) and the result in Eq. (52), respectively. At the current level of precision, the shapes of the inclusive and exclusive decay rates are compatible with each other. Detailed studies of decay-rate shapes could in the future, when higher-precision theory predictions are available, allow us to shed light on possible discrepancies between inclusive and exclusive CKM determinations.

3. R ratios

A second, very important application is to test lepton flavor universality (LFU). LFU is an accidental symmetry in the SM, and it is extremely important to test if it holds. One test is to compare these semileptonic decays with electron (e), muon (μ), or tau (τ) leptons in the final state. In the SM, their couplings with gauge bosons (W, Z) are identical. However, since their masses differ, the shapes of the partial width distributions with respect to q^2 will be different, and so will be their integrated (or partially integrated) rates. Comparison of measured and predicted rates constitutes another important test of the SM. It is particularly interesting and important to take ratios of integrated rates which are manifestly independent of the mixing angles. Since the mixing angles are known within some uncertainty, LFU tests using the following ratios can be a powerful precision test. Traditionally, one introduces

$$R_{B_s\to K} = \frac{\int_{m_\tau^2}^{q^2_{\rm max}} dq^2 \frac{d\Gamma(B_s\to K\tau\bar{\nu}_\tau)}{dq^2}}{\int_{m_\ell^2}^{q^2_{\rm max}} dq^2 \frac{d\Gamma(B_s\to K\ell\bar{\nu}_\ell)}{dq^2}} \tag{53}$$

and takes the limit of integration from $q^2 = m^2_{\ell(\tau)}$ to the maximum value of q^2 that is kinematically allowed. In this equation, ℓ in the denominator stands for e or μ, whereas the numerator is for the tau lepton. Since the electron and

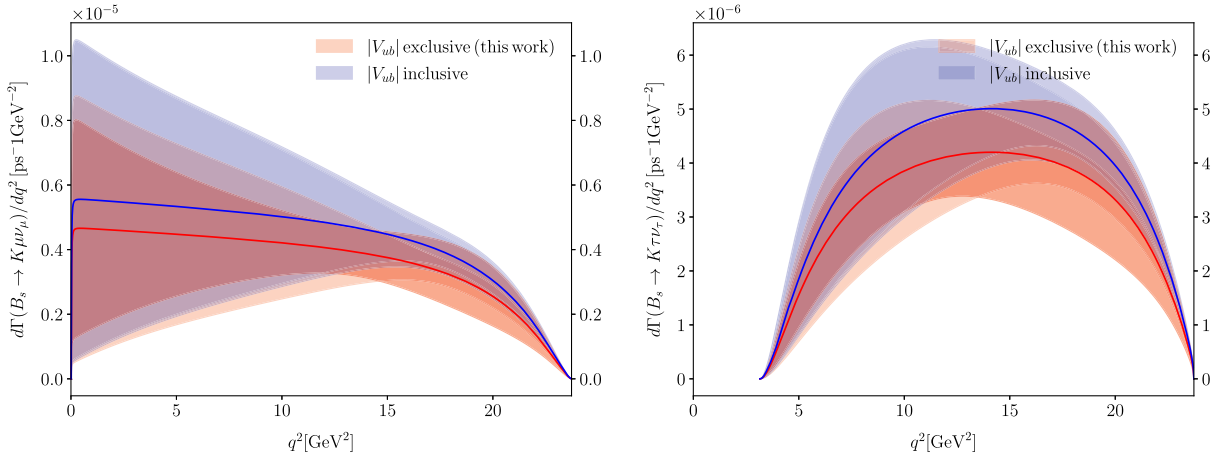

FIG. 9. The differential decay width $d\Gamma/dq^2$ for $B_s \to K\mu\bar{\nu}_\mu$ (left) and $B_s \to K\tau\bar{\nu}_\tau$ (right). The values for $|V_{ub}|$ are taken from Eqs. (50) and (52). The darker (lighter) shading indicates the error without (with) the contribution from the error on $|V_{ub}|$.

muon masses are negligible compared to the mass of the parent B_s, the contribution to the denominator from the form factor f_0 is tiny since it is proportional to the lepton mass in the amplitude. This means that for the numerator involving decays to τ, the contribution from the scalar form factor f_0 cannot be determined experimentally from data for the semileptonic decays into e or μ. The scalar form factor must be calculated from theory in a nonperturbative framework. This realization motivated lattice studies long ago [111].

The conventional definition of $R_{B_s\to K}$ in Eq. (53) has a drawback. The contribution to the denominator from $m_\ell^2 \le q^2 \le m_\tau^2$ has no corresponding contribution in the numerator; thus, that region does not give useful information for testing LFU. To emphasize this, imagine $d\Gamma/dq^2$ is very peaked for small q^2. Then, the conventional $R_{B_s\to K}$, given in (53), would tend to be very small, providing little useful information.

Following Refs. [112,113], we propose to use another ratio (cf. Ref. [114]) where we:

(i) use a common integration range in the numerator and denominator, with lower limit $q^2_{\rm min} \ge m_\tau^2$ (changing the lower limit was proposed earlier in Refs. [115,116] as well as in Ref. [113]),

(ii) make the weights multiplying the form factor terms involving $f_+(q^2)$ in the integrands the same for τ and ℓ modes (as in Ref. [113]).

To do this, we rewrite the differential decay rate in Eq. (1) in the form

$$\frac{d\Gamma(B_s \to K\ell\nu)}{dq^2} = \Phi\omega_\ell(q^2)[F_V^2 + (F_S^\ell)^2], \tag{54}$$

where ℓ can be any of e, μ, τ and

$$\Phi = \eta_{\rm EW}\frac{G_F^2|V_{ub}|^2}{24\pi^3}, \tag{55}$$

$$\omega_\ell(q^2) = \left(1-\frac{m_\ell^2}{q^2}\right)^2\left(1+\frac{m_\ell^2}{2q^2}\right), \tag{56}$$

$$F_V^2 = |\mathbf{p}_K|^3|f_+(q^2)|^2, \tag{57}$$

$$(F_S^\ell)^2 = \frac{3}{4}\frac{m_\ell^2|\mathbf{p}_K|}{m_\ell^2+2q^2}\frac{(M_{B_s}^2-M_K^2)^2}{M_{B_s}^2}|f_0(q^2)|^2. \tag{58}$$

The subscript ℓ on ω_ℓ and superscript ℓ in $(F_S^\ell)^2$ show where the dependence on the lepton mass enters. The improved R ratio is now defined by

$$R^{\rm imp}_{B_s\to K} = \frac{\int_{q^2_{\rm min}}^{q^2_{\rm max}} dq^2 \frac{d\Gamma(B_s\to K\tau\bar{\nu}_\tau)}{dq^2}}{\int_{q^2_{\rm min}}^{q^2_{\rm max}} dq^2 [\frac{\omega_\tau(q^2)}{\omega_\ell(q^2)}]\frac{d\Gamma(B_s\to K\ell\nu)}{dq^2}}, \tag{59}$$

where ℓ in the denominator is once again e or μ. With instead a vector meson in the final state, this matches the definition in Ref. [113]. The ratio can be evaluated using experimentally measured differential decay rates. We propose using this ratio as a way to monitor LFU.

We can evaluate the ratio $R^{\rm imp}_{B_s\to K}$ from the Standard Model using our lattice determinations of the form factors. In the approximation in which we drop the scalar form factor contribution in the denominator [in (58), $m_{e,\mu}^2/2q^2 \le m_\mu^2/2q^2 \le m_\mu^2/2m_\tau^2 = 0.002$ in the integration range], we have

$$R^{\rm imp,SM}_{B_s\to K} \approx 1 + \frac{\int_{q^2_{\rm min}}^{q^2_{\rm max}} dq^2\omega_\tau(q^2)(F_S^\tau)^2}{\int_{q^2_{\rm min}}^{q^2_{\rm max}} dq^2\omega_\tau(q^2)F_V^2}, \tag{60}$$

where now both numerator and denominator have the same weight.

Results for both $R_{B_s\to K}$ and $R^{\rm impr}_{B_s\to K}$. are listed in Table XI, where we also include our result for the integrated decay rate $\Gamma/|V_{ub}|$. As above, only the results for $K_{+,0} \geq 3$ should be considered to be free of truncation errors in the z expansion. The error we achieve on the new ratio is about three times smaller than for the old ratio. Here is a summary of our central results (based on $(K_+, K_0) = (5, 5)$):

$$R_{B_s\to K} = 0.77(16), \tag{61}$$

$$R^{\rm impr}_{B_s\to K} = 1.72(11). \tag{62}$$

4. Forward-backward and polarization asymmetries

Starting from the differential decay rate in terms of the lepton angle θ_ℓ between the charged-lepton and B_s momentum in the q^2 rest frame, our form factor data also allows us to compute the forward-backward asymmetry. The forward-backward difference is given by

$$\mathcal{A}^\ell_{\rm FB}(q^2) \equiv \left[\int_0^1 - \int_{-1}^0\right] d\cos\theta_\ell \frac{d^2\Gamma(B_s \to K\ell\nu)}{dq^2 d\cos\theta_\ell}, \tag{63}$$

and in the SM, it takes the form [117]

$$\mathcal{A}^\ell_{\rm FB}(q^2) = \eta_{\rm EW}\frac{G_F^2|V_{ub}|^2}{32\pi^3 M_{B_s}}\left(1-\frac{m_\ell^2}{q^2}\right)^2|\mathbf{p}_K|^2 \times \frac{m_\ell^2}{q^2}(M_{B_s}^2 - M_K^2) f_+(q^2) f_0(q^2). \tag{64}$$

A probe for helicity-violating interactions is provided by the difference of the left-handed and right-handed contributions to the decay rate [117]

$$\mathcal{A}^\ell_{\rm pol}(q^2) = \frac{d\Gamma(\ell, \mathrm{LH})}{dq^2} - \frac{d\Gamma(\ell, \mathrm{RH})}{dq^2}, \tag{65}$$

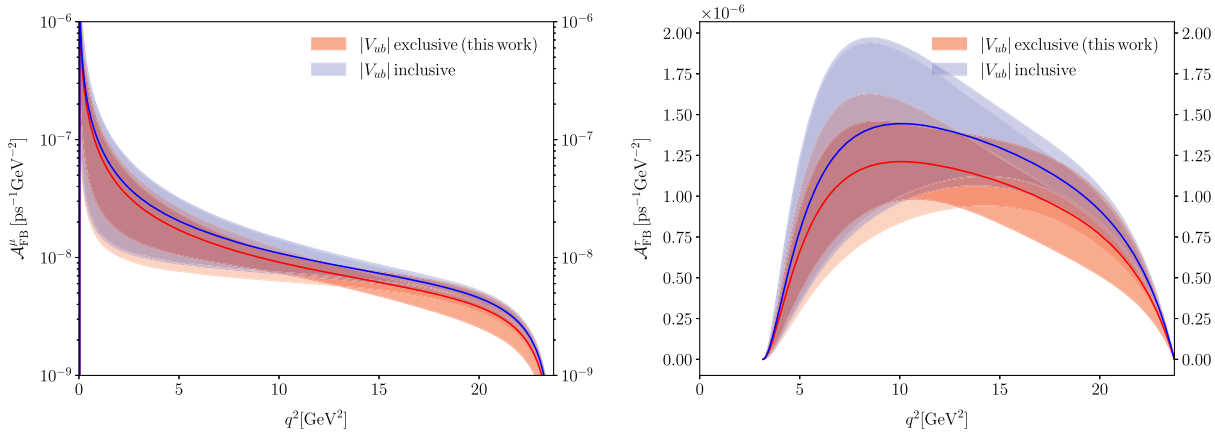

FIG. 10. Forward-backward asymmetries $\mathcal{A}^\mu_{\rm FB}$ (left) and $\mathcal{A}^\tau_{\rm FB}$ (right). For convenient visualization, the left-hand plot is shown on a logarithmic scale. The values for $|V_{ub}|$ are taken from Eqs. (50) and (52). The darker (lighter) shading indicates the error without (with) the contribution from the error on $|V_{ub}|$.

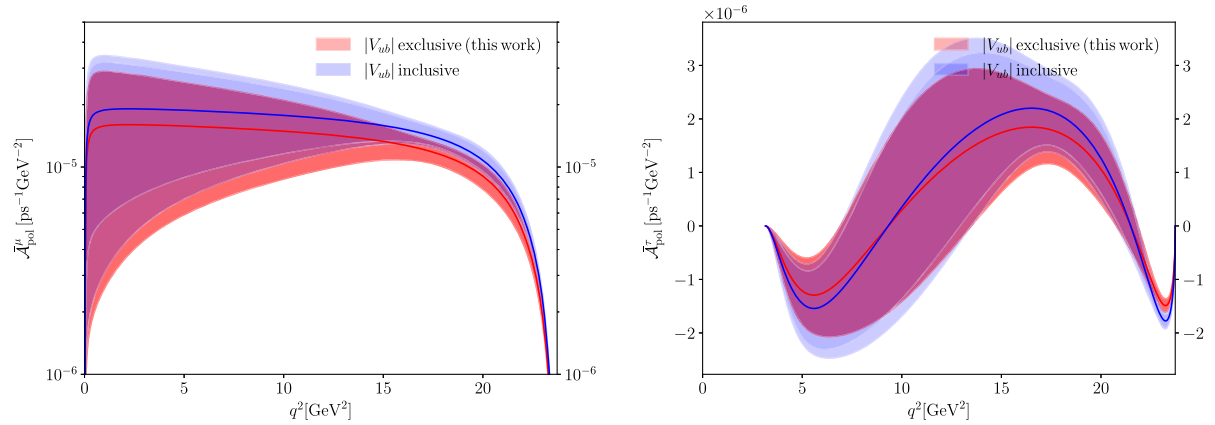

FIG. 11. Difference of the left-handed and right-handed contributions to the decay rate $\mathcal{A}^\mu_{\rm pol}$ (left) and $\mathcal{A}^\tau_{\rm pol}$ (right). The values for $|V_{ub}|$ are taken from Eqs. (50) and (52). The darker (lighter) shading indicates the error without (with) the contribution from the error on $|V_{ub}|$.

TABLE XII. Results for observables based on the results for the z fits in Table X. The main results of this paper are the ones with $(K_+, K_0) = (5, 5)$.

K_+	K_0	$I(\mathcal{A}^\tau_{\rm FB})$ $(\frac{1}{\rm ps})$	$I(\mathcal{A}^\mu_{\rm FB})$ $(\frac{1}{\rm ps})$	$\bar{\mathcal{A}}^\tau_{\rm FB}$	$\bar{\mathcal{A}}^\mu_{\rm FB}$	$I(\mathcal{A}^\tau_{\rm pol})$ $(\frac{1}{\rm ps})$	$I(\mathcal{A}^\mu_{\rm pol})$ $(\frac{1}{\rm ps})$	$\bar{\mathcal{A}}^\tau_{\rm pol}$	$\bar{\mathcal{A}}^\mu_{\rm pol}$
2	2	1.46(12)	0.0320(46)	0.2720(21)	0.00440(27)	0.794(92)	7.16(68)	0.148(13)	0.98768(73)
2	3	0.99(14)	0.0115(41)	0.2679(27)	0.00284(46)	0.31(13)	3.90(80)	0.082(27)	0.9912(11)
3	2	1.23(13)	0.0315(46)	0.2825(28)	0.00560(44)	0.14(15)	5.53(71)	0.031(34)	0.9838(13)
3	3	1.27(23)	0.038(19)	0.2836(77)	0.0058(15)	0.13(16)	6.0(1.7)	0.030(35)	0.9833(39)
3	4	1.28(27)	0.040(26)	0.2833(91)	0.0057(19)	0.14(17)	6.1(2.2)	0.030(38)	0.9834(49)
4	3	1.29(26)	0.038(19)	0.2820(80)	0.0058(16)	0.18(31)	6.2(2.0)	0.034(65)	0.9832(45)
4	4	1.28(28)	0.039(25)	0.2817(93)	0.0058(20)	0.16(31)	6.2(2.4)	0.031(64)	0.9833(52)
5	5	1.30(28)	0.040(24)	0.2821(89)	0.0057(18)	0.18(29)	6.3(2.3)	0.035(60)	0.9834(49)
6	6	1.31(28)	0.041(24)	0.2826(88)	0.0058(18)	0.19(29)	6.4(2.3)	0.036(58)	0.9832(48)
7	7	1.33(28)	0.043(24)	0.2831(85)	0.0060(18)	0.20(31)	6.6(2.4)	0.037(62)	0.9829(47)
8	8	1.34(29)	0.043(25)	0.2827(86)	0.0059(18)	0.23(32)	6.7(2.5)	0.042(64)	0.9831(47)
9	9	1.35(31)	0.045(27)	0.2830(90)	0.0060(18)	0.23(34)	6.8(2.6)	0.041(67)	0.9827(49)
10	10	1.37(31)	0.047(27)	0.2832(93)	0.0062(18)	0.23(36)	7.0(2.7)	0.040(69)	0.9823(49)

where

$$\frac{d\Gamma(\ell, \mathrm{LH})}{dq^2} = \eta_{\rm EW}\frac{G_F^2|V_{ub}|^2|\mathbf{p}_K|^3}{24\pi^3}\left(1-\frac{m_\ell^2}{q^2}\right)^2 f_+^2(q^2),$$
$$\frac{d\Gamma(\ell, \mathrm{RH})}{dq^2} = \eta_{\rm EW}\frac{G_F^2|V_{ub}|^2|\mathbf{p}_K|}{24\pi^3}\frac{m_\ell^2}{q^2}\left(1-\frac{m_\ell^2}{q^2}\right)^2 \times\left(\frac{3}{8}\frac{(M_{B_s}^2-M_K^2)^2}{M_{B_s}^2}f_0^2(q^2)+\frac{1}{2}|\mathbf{p}_K|^2 f_+^2(q^2)\right). \tag{66}$$

We show our results for the forward-backward asymmetries and the polarization distribution in Figs. 10 and 11, respectively, where the case $\ell = \mu$ (τ) is shown in the left (right) panel. In Table XII, we provide numerical results for

$$I[\mathcal{A}^\ell] = \int_{m_\ell^2}^{q^2_{\rm max}} dq^2 \mathcal{A}^\ell(q^2)/|V_{ub}|^2, \tag{67}$$

and

$$\bar{\mathcal{A}}^\ell = \frac{\int_{m_\ell^2}^{q^2_{\rm max}} dq^2 \mathcal{A}^\ell(q^2)}{\int_{m_\ell^2}^{q^2_{\rm max}} dq^2 d\Gamma(B_s\to K\ell\nu)/dq^2}, \tag{68}$$

where $\mathcal{A}^\ell = \mathcal{A}^\ell_{\rm FB}, \mathcal{A}^\ell_{\rm pol}$. Here is a summary of our central results $[(K_+, K_0) = (5, 5)]$:

$$I[\mathcal{A}^\tau_{\rm FB}] = 1.30(28)\ \mathrm{ps}^{-1}, \tag{69}$$
$$I[\mathcal{A}^\mu_{\rm FB}] = 0.040(24)\ \mathrm{ps}^{-1}, \tag{70}$$
$$\bar{\mathcal{A}}^\tau_{\rm FB} = 0.2821(89), \tag{71}$$
$$\bar{\mathcal{A}}^\mu_{\rm FB} = 0.0057(18), \tag{72}$$
$$I[\mathcal{A}^\tau_{\rm pol}] = 0.18(29)\ \mathrm{ps}^{-1}, \tag{73}$$
$$I[\mathcal{A}^\mu_{\rm pol}] = 6.3(2.3)\ \mathrm{ps}^{-1}, \tag{74}$$
$$\bar{\mathcal{A}}^\tau_{\rm pol} = 0.035(60), \tag{75}$$
$$\bar{\mathcal{A}}^\mu_{\rm pol} = 0.9834(49), \tag{76}$$

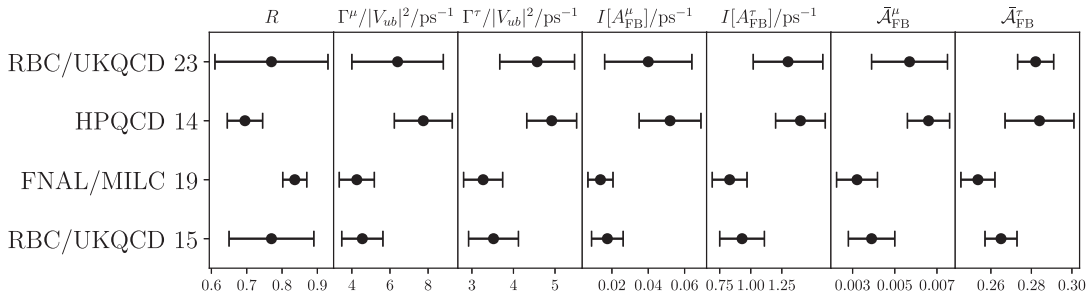

FIG. 12. Comparison with results from other collaborations (HPQCD 14 [8], RBC/UKQCD 15 [10], FNAL/MILC 19 [11], and this work, RBC/UKQCD 23).

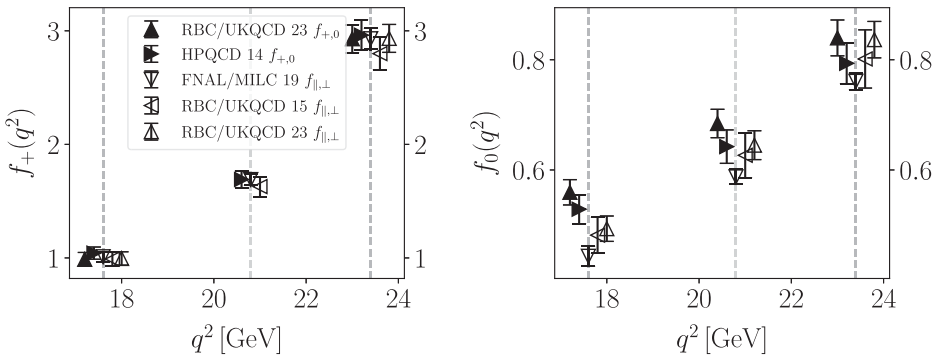

FIG. 13. Summary of available lattice data for the $B_s \to K\ell\nu$ form factors f_+ (left) and f_0 (right) at the same arbitrarily chosen reference points indicated by dashed vertical lines (to improve the presentation, individual data points are shifted slightly in q^2). Empty symbols indicate the results where the chiral and continuum extrapolations have been carried out in terms of $f_\perp$ and $f_\parallel$ and then converted to f_+ and f_0 using Eqs. (5) and (4), respectively. The points for RBC/UKQCD 23 $f_{\parallel,\perp}$ were generated solely for the purpose of illustration, using the data and analysis methods discussed in this paper, but with the chiral and continuum extrapolation done for $f_\parallel$ and $f_\perp$. Filled symbols indicate the results where the extrapolation has been done in terms of f_+ (left) and f_0 (right).

and in Fig. 12, we provide a comparison with results from other lattice simulations. Two observations are worth highlighting: with respect to RBC/UKQCD 15, some of the results shifted significantly, and the error of some results increased visibly. The shift is mainly down to our decision to do the HMχPT chiral and continuum limit for f_+ and f_0 rather than for $f_\perp$ and $f_\parallel$. The assumption that the same pole masses simultaneously describes the momentum dependence of f_+ and $f_\perp$ and f_0 and $f_\parallel$, respectively, does not seem correct at the level of precision we achieve with our dataset. The increase in error on the other hand is due to the change in strategy for the BGL parametrization—at the cost of achieving a truncation-independent parametrization of the form factor, the statistical error on observables particularly sensitive to the low-q^2 behavior of the form factor increases.

VI. CONCLUSIONS

In this paper, we present our new results for the nonperturbative Standard Model contributions to the exclusive semileptonic decay $B_s \to K\ell\nu$. In particular, we present the results for the form factors $f_+(q^2)$ and $f_0(q^2)$ in the continuum limit of $N_f = 2+1$ lattice simulations. We have improved our analysis in various ways: a) we have improved the control of the continuum limit by including simulations on a finer ($a^{-1} \approx 2.8$ GeV) ensemble; b) we include the effects of excited states in our correlation function fits; c) doing the chiral-continuum extrapolation of f_+ and f_0 rather than $f_\parallel$ and $f_\perp$ using HMχPT removes an otherwise irreducible systematic effect present in earlier work [10,11], which might be the origin of tensions in the combined analysis of lattice results [15]; d) using the Bayesian-inference approach to fitting the z-parametrization proposed in Ref. [95], we obtain a model- and truncation-independent parametrization of the form factor in the entire physical semileptonic kinematical range.

Regarding point c, we summarize the situation of available lattice data for the $B_s \to K\ell\nu$ form factors in Fig. 13. While all available data for the vector form factor f_+ are in agreement, the data for f_0 show two clusters of data points forming as q^2 is reduced. The two clusters can be distinguished by the way in which the chiral and continuum limit have been taken. In our view, taking the continuum limit in terms of f_+ and f_0 rather than in in terms of $f_\perp$ and $f_\parallel$ is correct. The same note of caution concerns other quantities like, e.g., $B \to \pi\ell\nu$, where very similar analysis techniques are being used.

We use our results to make a number of predictions for phenomenology. In particular, we make a new prediction for the CKM matrix element $|V_{ub}| = 3.78(61) \times 10^{-3}$ based on first results for the $B_s \to K\ell\nu$ decay from the LHCb experiment [16]. The error is dominated by the experimental uncertainty. In particular, if we repeat the analysis with the experimental uncertainty set to zero, the error on $|V_{ub}|$ reduces to 0.37. Our result is compatible with both exclusive and inclusive determinations. We also make predictions for the shape of the differential decay rate, the forward-backward asymmetry, and the difference between left-handed and right-handed contributions to the decay rate. With more precise experimental and lattice results, these observables might in the future allow us to shed light on the tension between inclusive and exclusive $|V_{ub}|$ determinations.

ACKNOWLEDGMENTS

We thank our RBC/UKQCD collaborators for helpful discussions and suggestions, Paolo Gambino for discussion on unitarity-constrained fits, and Greg Ciezarek for discussions of the LHCb form-factor data. We thank Edwin Lizarazo for contributions at early stages of this work. Computations used resources provided by the USQCD Collaboration, funded by the Office of Science of the U.S.

Department of Energy and by the ARCHER UK National Supercomputing Service, as well as computers at Columbia University, Brookhaven National Laboratory, and the OMNI cluster of the University of Siegen. This document was prepared using the resources of the USQCD Collaboration at the Fermi National Accelerator Laboratory (Fermilab), a U.S. Department of Energy (DOE), Office of Science, HEP User Facility. Fermilab is managed by Fermi Research Alliance, LLC (FRA), acting under Contract No. DE-AC02-07CH11359. This work used the DiRAC Extreme Scaling service at the University of Edinburgh, operated by the Edinburgh Parallel Computing Centre on behalf of the STFC DiRAC HPC Facility. This equipment was funded by BEIS capital funding via STFC capital Grant No. ST/R00238X/1 and STFC DiRAC Operations Grant No. ST/R001006/1. DiRAC is part of the National e-Infrastructure. We used gauge-field configurations generated on the DiRAC Blue Gene Q system at the University of Edinburgh, part of the DiRAC Facility, funded by BIS National E-infrastructure Grant No. ST/K000411/1 and STFC Grants No. ST/H008845/1, No. ST/K005804/1, and No. ST/K005790/1. We thank BNL, Fermilab, the Columbia University, the University of Edinburgh, the University of Siegen, the STFC, and the U.S. DOE for providing the facilities essential for the completion of this work. This project has received funding from Marie Skłodowska-Curie Grants No. 659322 and 894103 (EU Horizon 2020) and U.K. STFC Grant No. ST/P000630/1 and is supported by the Deutsche Forschungsgemeinschaft (DFG, German Research Foundation) through Grant No. 396021762—TRR 257 "Particle Physics Phenomenology after the Higgs Discovery." The work of A. S. was supported in part by the U.S. DOE Contract No. DE-SC0012704.

APPENDIX A: RHQ PARAMETER TUNING

Here, we summarize the nonperturbative tuning of the three parameters in the RHQ action used for b-quarks. The procedure is described in Ref. [33], based on lattice spacings determined in Ref. [20]. The lattice spacing is a crucial input and with updated and refined global fits available [21,22,29], plus new ensembles, we have performed a new tuning for the ensembles used here. More precise determinations of the lattice spacings lead to reduced systematic errors in the RHQ parameters. In addition, the values for the strange-quark mass have been reanalyzed, and we have generated new valence-quark propagators with mass tuned or close to the updated strange-quark mass.

1. Nonperturbative tuning procedure

The parameters in the RHQ action, $\{m_0a, c_P, \zeta\}$, are fixed by demanding that the action correctly describes experimentally measured on-shell B_s-meson properties. We match the experimental values [75] of the spin-averaged mass and the hyperfine splitting and require that the rest and kinetic masses of the B_s are equal

$$\bar{M}_{B_s} = \frac{M_{B_s} + 3M_{B_s^*}}{4}, \qquad \Delta M_{B_s} = M_{B_s^*} - M_{B_s}, \qquad \frac{M_1^{B_s}}{M_s^{B_s}} = 1. \tag{A1}$$

The latter implies that the B_s meson satisfies the continuum dispersion relation, $E_{B_s}^2(\mathbf{p}) = \mathbf{p}^2 + M_{B_s}^2$. We calculate the quantities above using seven sets of choices for the RHQ parameters $\{m_0a, c_P, \zeta\}$ and then make a linear interpolation to find the values satisfying the matching conditions above. The seven choices, indexed 1 to 7 from left to right, comprise a central set plus variations of each of the three parameters:

$$\begin{bmatrix} m_0a \\ c_P \\ \zeta \end{bmatrix}, \begin{bmatrix} m_0a - \sigma_{m_0a} \\ c_P \\ \zeta \end{bmatrix}, \begin{bmatrix} m_0a + \sigma_{m_0a} \\ c_P \\ \zeta \end{bmatrix}, \begin{bmatrix} m_0a \\ c_P - \sigma_{c_P} \\ \zeta \end{bmatrix}, \begin{bmatrix} m_0a \\ c_P + \sigma_{c_P} \\ \zeta \end{bmatrix}, \begin{bmatrix} m_0a \\ c_P \\ \zeta - \sigma_\zeta \end{bmatrix}, \begin{bmatrix} m_0a \\ c_P \\ \zeta + \sigma_\zeta \end{bmatrix}. \tag{A2}$$

We make a constant-plus-linear ansatz for the dependence of the observables on the RHQ parameters

$$\begin{bmatrix} \bar{M}_{B_s} \\ \Delta M_{B_s} \\ M_1^{B_s}/M_2^{B_s} \end{bmatrix} = J \cdot \begin{bmatrix} m_0a \\ c_P \\ \zeta \end{bmatrix} + A. \tag{A3}$$

Here, J represents the "slope" and is a 3×3 matrix, while A corresponds to the intercept and is a 3×1 vector. In a region with sufficiently linear dependence on the parameters, we can obtain J and A using finite differences to approximate derivatives:

$$J = \left[\frac{Y_3 - Y_2}{2\sigma_{m_0a}}, \frac{Y_5 - Y_4}{2\sigma_{c_P}}, \frac{Y_7 - Y_6}{2\sigma_\zeta} \right],$$
$$A = Y_1 - J \cdot [m_0a, c_P, \zeta]^T. \tag{A4}$$

The vectors Y_i are constructed from the values of meson masses and splittings measured on the ith parameter set in (A2),

$$Y_i = [\bar{M}_{B_s}, \Delta M_{B_s}, M_1^{B_s}/M_2^{B_s}]_i^T. \tag{A5}$$

Inverting Eq. (A3), we obtain the tuned RHQ parameters

TABLE XIII. Input strange-quark mass am_s, width σ_G, and iteration count N_G of the Gaussian source smearing used to calculate $B_s^{(*)}$ meson two-point functions. We extract the $B_s^{(*)}$ energies by performing correlated fits using the specified fit ranges. The optimal Gaussian source-smearing radius was explored for the C and M ensembles in Ref. [33], and we scaled those results to the finer lattice spacing $a^{-1} = 2.785$ GeV on the F1S ensemble.

	a^{-1}/GeV	L^3	$a(m_s + m_{\text{res}})$	σ_G	N_G	Fit range
C	1.785	24^3	$0.03224 + 0.00315$	7.86	100	[10:25]
M	2.383	32^3	$0.025 + 0.00067$	10.36	170	[12:21]
F	2.785	48^3	$0.02144 + 0.00094$	12.14	230	[14:29]

$$\begin{bmatrix} m_0 a \\ c_P \\ \zeta \end{bmatrix}^{\text{RHQ}} = J^{-1} \cdot \left(\begin{bmatrix} \bar{M}_{B_s} \\ \Delta M_{B_s} \\ M_1^{B_s}/M_2^{B_s} \end{bmatrix}^{\text{PDG}} - A \right), \quad \text{(A6)}$$

by matching to PDG values and demanding the B_s rest mass equals its kinetic mass. Specifically, we use [75].

$$\begin{aligned} \bar{M}_{B_s} &= \frac{1}{4}(5366.82^{+0.22}_{-0.22} + 3 \cdot 5415.4^{+1.8}_{-1.4})\ \text{MeV} \\ &= 5403.26^{+1.8}_{-1.4}\ \text{MeV}, \\ \Delta M_{B_s} &= 48.6^{+1.8}_{-1.6}\ \text{MeV}. \end{aligned} \quad \text{(A7)}$$

We conservatively use the full error on $M_{B_s^*}$ as the uncertainty of the spin-averaged mass. The relative error on $\Delta_{M_{B_s}}$ is much larger and will dominate systematic effects due to the experimental inputs. These inputs are updated from those in Ref. [118] used in Ref. [33].

2. Lattice simulations

The tuning procedure is implemented by first determining $B_s^{(*)}$-meson energies for zero and nonzero momenta on our set of ensembles in Table I. We calculate two-point functions by contracting strange-quark propagators using point source and point sink with Gaussian source-smeared, point-sink b-quark propagators and extract $B_s^{(*)}$-meson energies from correlated fits to the plateau of effective energies. We find good correlated confidence levels (p-value $\gtrsim 10\%$) in all cases, and varying the fitting range by ± 1 time slice changes the result only within the statistical uncertainty. The value of our input strange-quark mass as well as the width σ_G and the number of iterations N_G for the Gaussian source smearing of the b-quarks are summarized in Table XIII together with the fitting range used to extract the $B_s^{(s)}$ meson energies.

Starting from the tuning performed in Ref. [33], we iterate twice to find the new central set of RHQ parameters for the C and M ensembles and choose roughly three times the size of the statistical errors for the variations $\sigma_{\{m_0 a, c_P, \zeta\}}$. For the new F1S ensemble at the finer lattice spacing, we roughly scaled our new results on C and M ensembles and then carried out two iterations choosing variations $\sigma_{\{m_0 a, c_P, \zeta\}}$ of roughly 1.5 times the statistical uncertainties. In all cases, our final parameter sets allow us to interpolate to the values of $m_0 a$, c_P, and ζ describing physical b-quarks, and we do not observe any signs of curvature within the explored parameter ranges. The final values of the central parameter sets and their variations are listed in Table XIV. Using those values, we determine spin-averaged masses, hyperfine splittings, and ratios of rest mass over kinetic mass in order to match to experimental results reported by the Particle Data Group (PDG) as in Eq. (A7). We finally obtain our tuned parameters from Eq. (A6). For the C and M ensembles, we cannot resolve a dependence on the light sea-quark mass within statistical errors. Hence, we average the values at the same lattice spacing. We report these results, plus the outcome for tuning on the F1S ensemble, in Table XV.

TABLE XIV. Central parameter set $\{m_0 a, c_P, \zeta\}$ with variations $\sigma_{m_0 a}, \sigma_{c_P}, \sigma_\zeta$ for the final iteration of tuning the parameters on C, M, and F ensembles with inverse lattice spacings ranging from 1.785 to 2.785 GeV.

	a^{-1}/GeV	L^3	$m_0 a \pm \sigma_{m_0 a}$	$c_P \pm \sigma_{c_P}$	$\zeta \pm \sigma_\zeta$
C	1.785	24^3	7.42 ± 0.18	4.86 ± 0.42	2.92 ± 0.21
M	2.383	32^3	3.46 ± 0.09	3.03 ± 0.24	1.75 ± 0.10
F	2.785	48^3	2.35 ± 0.20	2.75 ± 0.30	1.50 ± 0.15

TABLE XV. Tuned RHQ parameter values for all lattices determined using the parameter sets specified in Table XIV. For the C and M lattices, we see no dependence on the light sea-quark mass within statistical errors, and we consequently compute weighted averages to obtain our preferred values.

am_l	$m_0 a$	c_P	ζ
	C: $a^{-1} = 1.785$ GeV, $24^3 \times 64$		
0.005	7.468(66)	4.87(18)	2.922(82)
0.010	7.476(80)	4.97(19)	2.94(10)
average	7.471(51)	4.92(13)	2.929(63)
	M: $a^{-1} = 2.383$ GeV, $32^3 \times 64$		
0.004	3.541(46)	3.19(13)	1.715(55)
0.006	3.474(37)	3.01(10)	1.759(46)
0.008	3.444(48)	3.02(14)	1.807(55)
average	3.485(25)	3.063(69)	1.760(30)
	F: $a^{-1} = 2.785$ GeV, $48^3 \times 96$		
0.002144	2.423(62)	2.68(13)	1.523(79)

3. Estimating systematic uncertainties

a. Heavy-quark-discretization errors

When $m_0 a \sim 1$, the RHQ action leads to a nontrivial lattice-spacing dependence of physical quantities. As discussed in detail in Ref. [33], we estimate the discretization errors for the heavy sector using power counting, following Oktay and Kronfeld [119]. Since we are considering the same physical quantities, spin-averaged mass, hyperfine splitting, and ratio of rest over kinetic mass, we simply list uncertainties in percent and refer to Appendix C of Ref. [33] for further details:

$$\begin{aligned} \text{error}_{\text{total}}^{M_{1,B_s}} &= 0.05\%, \\ \text{error}_{\text{total}}^{M_{2,B_s}} &= 2.59\%, \\ \text{error}_{\text{total}}^{\Delta M_{B_s}} &= 4.40\%. \end{aligned} \tag{A8}$$

By assigning these errors as uncertainty in our inputs to the matching procedure, we propagate them to the RHQ parameters and collect the percentage changes in the central values in the first panel of Table XVI.

b. Input strange-quark mass

Our RHQ parameters are tuned using strange-quark propagators corresponding to a mass at or near the physical strange-quark mass. We need to account for slight mistunings as well as for the uncertainty in the strange-quark mass quoted in Refs. [21,22] (see also Table I).

On the coarse (C) ensembles, we can bracket the strange-quark mass using the additional quark propagators with bare masses $am_s' = 0.03$ and 0.04. This allows us to determine numerically the slopes of m_0, c_P, and ζ with respect to the strange-quark mass. Since the mass of our strange-quark propagators matches the physical value, we read off the changes in $m_0 a$, c_P, and ζ after varying am_s by $\pm 1\sigma$. The largest change we observe is 0.2%.

TABLE XVI. Systematic uncertainties in percent with a significant effect on our tuned RHQ parameters. For the C and M ensembles, we always report the largest fluctuation observed on either ensemble.

Uncertainty	a^{-1}/GeV	$m_0 a$	c_P	ζ
Heavy quark discretization	1.785	1.0%	5.6%	3.4%
	2.383	1.1%	6.0%	3.3%
	2.785	1.5%	5.6%	2.8%
Lattice scale	1.785	1.1%	1.4%	0.5%
	2.383	1.3%	1.7%	0.4%
	2.785	1.3%	1.4%	0.3%
Experiment	1.785	0.6%	4.8%	0.1%
	2.383	0.9%	5.0%	0.1%
	2.785	1.2%	4.8%	0.1%

For the M ensembles, we simulate with a bare strange-quark mass of 0.025 which is roughly 1σ larger than the physical value. Using in addition $am_s' = 0.0272$, we determine the slopes with respect to m_s and estimate the error due to mistuning as well as the uncertainty in the strange-quark mass by varying the strange-quark mass by $\pm 2\sigma$. Our RHQ parameters change at most by 0.3%.

For the F1S ensemble, since the slopes with respect to am_s decrease as the lattice spacing decreases, we use for simplicity the average of the slopes obtained on the M ensembles to estimate the uncertainty due to the input strange quark mass for F1S. Here, our value for the mass of the strange quark is within 1σ of the physical value. Being conservative, we vary the strange-quark mass by $\pm 2\sigma$ and read off changes of the RHQ parameters of at most 0.2%.

Given that for all ensembles and all three RHQ parameters the uncertainty due to the strange-quark mass is 0.3% or less, we consider this effect negligible compared to the percent-level uncertainties arising from, for example, heavy-quark discretization errors.

c. Lattice scale uncertainty

The lattice scale enters our tuning procedure when we convert the experimental input data to lattice units. To propagate the uncertainty of the lattice spacings to our RHQ parameters, we repeat the analysis varying the lattice spacing by $\pm 1\sigma$. For the C and M ensembles, we take the largest fluctuation of a central value on either ensemble as our estimate.

d. Experimental uncertainty

We estimate the uncertainty due to the experimental inputs by varying both the spin-averaged mass and the hyperfine splitting by $\pm 1\sigma$ each and rerun our matching analysis. In practice, the uncertainty in the spin-averaged mass is negligible compared to the few-percent effect due to the uncertainty in the hyperfine splitting. We take the largest change of the central values at a given lattice spacing as our estimate for the corresponding uncertainty in our RHQ parameters.

4. Tuned RHQ parameters

We summarize our tuned RHQ parameters in Table XVII quoting our final results with all systematic errors found to be significant.

APPENDIX B: RHQ DISCRETIZATION ERRORS

We tune the parameters in the RHQ action nonperturbatively, such that the leading heavy-quark discretization errors from the action are $O(a^2)$. We use an $O(\alpha_s a)$-improved vector current and calculate the improvement coefficient to one loop; hence, the leading heavy-quark discretization errors from the current are of $O(\alpha_s^2 a, a^2)$. Table XVIII gives values for the "mismatch" functions at

TABLE XVII. Values of the tuned RHQ parameters with central values and statistical errors taken from Table XV and estimates for the systematic errors from Table XVI. Tuning determines the bare-quark mass, $m_0 a$; clover coefficient, c_P; and anisotropy parameter, ζ, in the RHQ action. Errors listed for $m_0 a$, c_P, and ζ are, from left to right, statistics, heavy-quark discretization errors, the lattice scale uncertainty, and the uncertainty due to the experimental measurement of the B_s meson hyperfine splitting, respectively. Other errors considered but found to be negligible are not shown.

	a^{-1}/GeV	$m_0 a$	c_P	ζ
C	1.785	7.471(51)(75)(82)(45)	4.92(13)(28)(07)(24)	2.929(63)(100)(15)(03)
M	2.383	3.485(25)(38)(45)(31)	3.06(07)(18)(05)(15)	1.760(30)(58)(07)(02)
F	2.785	2.423(62)(36)(31)(29)	2.68(13)(15)(04)(13)	1.523(79)(43)(05)(02)

each of our lattice spacings, from which we find and list in Table XIX the estimated heavy quark discretization errors from the five different operators in the action and current. We refer the reader to Sec. V.E and Appendix B of Ref. [38] for further details.

APPENDIX C: RENORMALIZATION AND IMPROVEMENT COEFFICIENTS

Table II summarizes the values of the renormalization constants $Z_A^{ll}(am_l)$.

TABLE XVIII. Values of the mismatch functions defined in Appendix B of Ref. [38] for the nonperturbatively tuned parameters of the RHQ action given in Table XVII. The tree-level coefficients f_E, f_{X_i}, and f_Y are known exactly. The two-loop coefficient $f_3^{[2]}$ is not known, so we use an ansatz based on the tree-level expression. The coupling $\alpha_s(a^{-1})$ needed to evaluate $f_3^{[2]}$ is taken to be a lattice mean-field coupling at the (inverse) lattice spacing scale (see the discussion of the perturbative calculations in Sec. II C).

	a^{-1}/GeV	$\alpha_s(a^{-1})$	f_E	f_{X_1}	f_{X_2}	f_Y	$f_3^{[2]}$
C	1.785	0.2320	0.0594	0.0848	0.1436	0.1358	0.0333
M	2.383	0.2155	0.0809	0.0966	0.1691	0.1721	0.0298
F	2.785	0.2083	0.1042	0.1101	0.1946	0.2056	0.0299

In Table XX, we give the residual renormalization factors and the improvement coefficients for the heavy-light currents with a heavy RHQ and a light domain-wall quark, computed at one-loop order [43] in mean-field improved perturbation theory.

Table XXI gives inputs used for numerical evaluation of the perturbatively calculated coefficients. Mean-field improvement uses values for the average gauge link, u. We use either the fourth root of the plaquette expectation value, denoted u_P, or the mean link in Landau gauge, u_L. We use two choices of strong coupling: a mean-field lattice $\overline{\text{MS}}$ strong coupling, $\alpha_{s,\text{lat}}^{\overline{\text{MS}}}$, or the continuum $\overline{\text{MS}}$ strong coupling, $\alpha_{s,\text{ctm}}^{\overline{\text{MS}}}$, both evaluated at the scale $\mu = a^{-1}$. For the Iwasaki gauge action used for our gauge field ensembles, the lattice strong coupling depends on the plaquette and rectangle expectation values $\langle P \rangle$ and $\langle R_1 \rangle$, respectively, quoted in Table XXI. For the continuum coupling, we use five-loop running from RUNDEC [120–122], starting from $\alpha^{(5)}(\bar{m}_b(\bar{m}_b)) = 0.2268$ at $\bar{m}_b(\bar{m}_b) = 4.163$ GeV (the same choice was made when using RUNDEC to compute $\bar{m}_b(2\text{ GeV})$ for evaluating the χ factors in the outer functions for BGL z-fits; see Appendix D). The perturbative results in Table XXI are the average of values from the four combinations of u and $\alpha_s^{\overline{\text{MS}}}$. The columns headed Δ give half of the spread in the values from the four combinations.

TABLE XIX. Percentage errors from mismatches in the action and current for the bottom quark. For this estimate, we calculate the mismatch functions for the non-perturbatively-tuned parameters of the RHQ action from Table XVII. We estimate the size of operators using HQET power counting with $\Lambda_{\text{QCD}} = 500$ MeV and $\alpha_s^{\overline{\text{MS}}}(a^{-1})$. To obtain the total, we add the individual errors in quadrature, including each contribution the number of times that operator occurs. Contribution E is counted twice, while 3 is counted twice for $f_\parallel$ and four times for $f_\perp$. The definitions of operators E, X_1, X_2, Y, and 3, and expressions for the mismatch functions, are given in Appendix B of Ref. [38].

			$O(a^2)$ error from action	$O(a^2)$ errors from current			$O(\alpha_s^2 a)$ error from current	Total/%	
	a^{-1}/GeV	$\alpha_s(a^{-1})$	E	X_1	X_2	Y	3	$f_\parallel$	$f_\perp$
C	1.785	0.2320	0.47	0.67	1.13	1.07	0.93	2.24	2.60
M	2.383	0.2155	0.36	0.43	0.74	0.76	0.63	1.53	1.77
F	2.785	0.2083	0.34	0.35	0.63	0.66	0.54	1.33	1.53

TABLE XX. Residual renormalization factors and operator improvement coefficients. We compute the ρ factors and the matching coefficients c_i^n at one loop in mean-field improved lattice perturbation theory [43]. They are evaluated for the tuned RHQ bare-quark mass $m_0 a$ at each lattice spacing (indicated by the letters C, M, and F in column headers; see Table I) and for the choices of the domain-wall height $M_5 = 1.8$ The values are an average from four combinations of mean link and strong coupling, with the columns headed Δ giving the spread in values from the four combinations.

	C $M_5 = 1.8$		M $M_5 = 1.8$		F $M_5 = 1.8$	
	value	Δ	value	Δ	value	Δ
ρ_{V_0}	1.0301	0.0115	1.0177	0.0059	1.0130	0.0041
ρ_{V_i}	0.9959	0.0019	0.9926	0.0022	0.9921	0.0019
c_t^3	0.0599	0.0092	0.0574	0.0073	0.0550	0.0064
c_t^4	−0.0120	0.0042	−0.0109	0.0030	−0.0101	0.0025
c_s^1	−0.0010	0.0006	−0.0015	0.0006	−0.0018	0.0006
c_s^2	0.0020	0.0021	0.0004	0.0011	−0.0001	0.0009
c_s^3	0.0512	0.0060	0.0497	0.0050	0.0478	0.0044
c_s^4	−0.0038	0.0020	−0.0022	0.0011	−0.0015	0.0008

TABLE XXI. Inputs for numerical evaluation of perturbatively computed coefficients at the three different lattice spacings in our ensembles.

	C	M	F
a^{-1}/GeV	1.785	2.383	2.785
β	2.13	2.25	2.31
$\langle P \rangle$	0.588011	0.615580	0.627970
$\langle R_1 \rangle$	0.343464	0.379841	0.396626
u_P	0.875682	0.885770	0.890194
u_L	0.843997	0.860991	0.868440
$m_0 a$	7.471	3.485	2.423
$\alpha_{s,\mathrm{lat}}^{\overline{\mathrm{MS}}}(a^{-1})$	0.2320	0.2155	0.2083
$\alpha_{s,\mathrm{ctm}}^{\overline{\mathrm{MS}}}(a^{-1})$	0.3226	0.2811	0.2633

APPENDIX D: BGL FITS

Here, we give expressions for the Blaschke factors and outer functions used in BGL fits to form factors.

The Blaschke factor $B_X(q^2)$ is chosen to vanish at the positions of subthreshold poles sitting between q^2_{max} and t_*, with t_* denoting the squared momentum transfer for the lowest two-particle production threshold. If there are n such poles with masses m_i and corresponding z-values $z_i = z(m_i^2; t_*, t_0)$, then

$$B_X(q^2) = \prod_{i=0}^{n-1} \frac{z - z_i}{1 - \bar{z}_i z} = \prod_{i=0}^{n-1} z(q^2; t_*, m_i^2), \tag{D1}$$

where $z = z(q^2; t_*, t_0)$ and $\bar{z}_i$ is the complex conjugate of z_i in the first form of the expression. The function $z(q^2; t_*, t_0)$ is defined in Eq. (32), and our choice for t_0 is given in Eq. (33). For $B_s \to K\ell\nu$ decays, the threshold is $M_B + M_\pi = 5.4175$ GeV, and there is a subthreshold pole at $M_{B^*} = 5.32471$ GeV [50] for f_+, but not for f_0 for which $M_{B^*(0^+)} = 5.63$ GeV [51][3] is above threshold.

The outer functions used in the parametrizations of f_+ and f_0 take the form [84,89,91][4]

$$\phi_+(q^2, t_0) = \sqrt{\frac{\eta_I}{48\pi\chi_{1^-}(0)}} \frac{r_q^{1/2}}{r_0^{1/2}} (r_q + r_0)(r_q + \sqrt{t_*})^{-5} \times (t_+ - q^2)^{3/4} (r_q + r_-)^{3/2}, \tag{D2}$$

$$\phi_0(q^2, t_0) = \sqrt{\frac{\eta_I t_+ t_-}{16\pi\chi_{0^+}(0)}} \frac{r_q^{1/2}}{r_0^{1/2}} (r_q + r_0)(r_q + \sqrt{t_*})^{-4} \times (t_+ - q^2)^{1/4} (r_q + r_-)^{1/2}, \tag{D3}$$

where we have set $r_q = \sqrt{t_* - q^2}$, $r_- = \sqrt{t_* - t_-}$, and $r_0 = \sqrt{t_* - t_0}$ [$t_\pm$ are defined after Eq. (32)]. The $\chi_J(0)$ come from evaluating the vacuum polarization function of two currents ($\bar{b}\gamma_\mu u$ and its Hermitian conjugate), while the η_I are isospin factors counting accessible isospin-related states when inserting a sum over states between the two currents in the vacuum polarization function (to derive the unitarity constraint on the form factors). For $B_s \to K\ell\nu$, we have $\eta_I = 1$.

The $\chi_J(0)$ have condensate contributions and perturbative parts. Expressions with the perturbative parts to two loops are given in Ref. [124], and three-loop perturbative contributions have been calculated by Grigo *et al.* in Ref. [125] (the expressions in Ref. [124] use pole masses, while those in Ref. [125] use $\overline{\mathrm{MS}}$ masses; we checked that they agree once the scheme conversion needed to relate them is used). For $B_s \to K\ell\nu$ decays, with $x = u$, $\chi_J(0)$ is evaluated using $u = m_x/m_b = 0$.

We evaluate the perturbative contributions using the results from Ref. [125] and following the procedure used in Ref. [123], with input $\overline{\mathrm{MS}}$ masses $\bar{m}_b(\bar{m}_b) = 4.163(16)$ GeV and $\bar{m}_c(3\ \mathrm{GeV}) = 0.986(13)$ GeV from Ref. [126], and $\alpha_s^{(5)}(\bar{m}_b(\bar{m}_b)) = 0.2268(23)$). To evaluate the condensate contribution for $B_s \to K\ell\nu$, we ran the b mass to $\bar{m}_b(2\ \mathrm{GeV}) = 4.95$ GeV using the RUNDEC package [120–122] and combined it with $\langle \bar{u}u \rangle_{\mu=2\ \mathrm{GeV}} = -(274\ \mathrm{MeV})^3$, from a weighted mean of $2+1+1$ and $2+1$ flavor estimates for $\Sigma^{1/3}$ in SU(2) in the 2021 FLAG review [15,127–134]), giving $\bar{m}_b \langle \bar{u}u \rangle = -0.102\ \mathrm{GeV}^4$.

[3]The $B^*(0^+)$ masses in the compilation in Ref. [72] span a range from 1.8% below to 2.2% above this value.

[4]These also agree with the expressions given in Eqs. (2.13) and (2.14) of Ref. [123], if expressed in terms of z and using the same t_* and t_0 as Ref. [123].

We took $\langle \alpha_s G^2 \rangle = 0.0635(35)$ GeV^4 from a sum rules average [135]. We find

$$\chi_{1^-}(0) = 6.03 \times 10^{-4}\ \text{GeV}^{-2}$$
$$\chi_{0^+}(0) = 1.48 \times 10^{-2}. \quad \text{(D4)}$$

The values of $\chi_J(0)$ and η_I are needed for checking or imposing the unitarity constraint on each form factor. If the constraint is not saturated, then their values do not affect the physical result of a z-fit since they are a normalization which can be absorbed by an overall factor in the fit coefficients.

In Ref. [103], the two susceptibilities were computed nonperturbatively,

$$\chi_{1^-}(0) = 4.45(1.16) \times 10^{-4}\ \text{GeV}^{-2},$$
$$\chi_{0^+}(0) = 2.04(0.20) \times 10^{-2}. \quad \text{(D5)}$$

We do not observe any significant changes in our results for observables when using these values instead of those in Eq. (D4).

[1] R. Aaij *et al.* (LHCb Collaboration), Measurement of Form-Factor-Independent Observables in the Decay $B^0 \to K^{*0}\mu^+\mu^-$, Phys. Rev. Lett. **111**, 191801 (2013).

[2] R. Aaij *et al.* (LHCb Collaboration), Test of Lepton Universality Using $B^+ \to K^+\ell^+\ell^-$ Decays, Phys. Rev. Lett. **113**, 151601 (2014).

[3] J. P. Lees *et al.* (*BABAR* Collaboration), Evidence for an Excess of $\bar{B} \to D^{(*)}\tau^-\bar{\nu}_\tau$ Decays, Phys. Rev. Lett. **109**, 101802 (2012).

[4] J. P. Lees *et al.* (*BABAR* Collaboration), Measurement of an excess of $\bar{B} \to D^{(*)}\tau^-\bar{\nu}_\tau$ decays and implications for charged Higgs bosons, Phys. Rev. D **88**, 072012 (2013).

[5] M. Huschle *et al.* (Belle Collaboration), Measurement of the branching ratio of $\bar{B} \to D^{(*)}\tau^-\bar{\nu}_\tau$ relative to $\bar{B} \to D^{(*)}\ell^-\bar{\nu}_\ell$ decays with hadronic tagging at Belle, Phys. Rev. D **92**, 072014 (2015).

[6] R. Aaij *et al.* (LHCb Collaboration), Measurement of the Ratio of Branching Fractions $\mathcal{B}(\bar{B}^0 \to D^{*+}\tau^-\bar{\nu}_\tau)/\mathcal{B}(\bar{B}^0 \to D^{*+}\mu^-\bar{\nu}_\mu)$, Phys. Rev. Lett. **115**, 111803 (2015); **115**, 159901(E) (2015).

[7] LHCb Collaboration, Measurement of lepton universality parameters in $B^+ \to K^+\ell^+\ell^-$ and $B^0 \to K^{*0}\ell^+\ell^-$ decays, arXiv:2212.09153.

[8] C. Bouchard, G. P. Lepage, C. Monahan, H. Na, and J. Shigemitsu, $B_s \to K\ell\nu$ form factors from lattice QCD, Phys. Rev. D **90**, 054506 (2014).

[9] C. J. Monahan, C. M. Bouchard, G. P. Lepage, H. Na, and J. Shigemitsu, Form factor ratios for $B_s \to K\ell\nu$ and $B_s \to D_s\ell\nu$ semileptonic decays and $|V_{ub}/V_{cb}|$, Phys. Rev. D **98**, 114509 (2018).

[10] J. M. Flynn, T. Izubuchi, T. Kawanai, C. Lehner, A. Soni, R. S. Van de Water, and O. Witzel (RBC/UKQCD Collaboration), $B \to \pi\ell\nu$ and $B_s \to K\ell\nu$ form factors and $|V_{ub}|$ from $2+1$-flavor lattice QCD with domain-wall light quarks and relativistic heavy quarks, Phys. Rev. D **91**, 074510 (2015).

[11] A. Bazavov *et al.* (Fermilab/MILC Collaboration), $B_s \to K\ell\nu$ decay from lattice QCD, Phys. Rev. D **100**, 034501 (2019).

[12] F. Bahr, D. Banerjee, F. Bernardoni, A. Joseph, M. Koren, H. Simma, and R. Sommer (ALPHA Collaboration), Continuum limit of the leading-order HQET form factor in $B_s \to K\ell\nu$ decays, Phys. Lett. B **757**, 473 (2016).

[13] O. Witzel, Lattice QCD (focus on Charm and Beauty form factors, $R(D^*)$, b- & c-quark masses), Proc. Sci., Beauty2019 (**2020**) 037 [arXiv:2002.01056].

[14] A. Lytle, Lattice $B \to D^{(*)}$ form factors, $R(D^{(*)})$, and $|V_{cb}|$, Proc. Sci., LATTICE2019 (**2020**) 228 [arXiv:2004.01132].

[15] Y. Aoki *et al.* (Flavour Lattice Averaging Group (FLAG) Collaboration), FLAG review 2021, Eur. Phys. J. C **82**, 869 (2022).

[16] R. Aaij *et al.* (LHCb Collaboration), First Observation of the Decay $B_s^0 \to K^-\mu^+\nu_\mu$ and Measurement of $|V_{ub}|/|V_{cb}|$, Phys. Rev. Lett. **126**, 081804 (2021).

[17] H. Na, C. M. Bouchard, G. P. Lepage, C. Monahan, and J. Shigemitsu (HPQCD Collaboration), $B \to Dl\nu$ form factors at nonzero recoil and extraction of $|V_{cb}|$, Phys. Rev. D **92**, 054510 (2015).

[18] A. Sirlin, Large $m(W)$, $m(Z)$ behavior of the $O(\alpha)$ corrections to semileptonic processes mediated by W, Nucl. Phys. **B196**, 83 (1982).

[19] C. Allton *et al.* (RBC/UKQCD Collaboration), Physical results from $2+1$ flavor domain wall QCD and SU(2) chiral perturbation theory, Phys. Rev. D **78**, 114509 (2008).

[20] Y. Aoki *et al.* (RBC/UKQCD Collaboration), Continuum limit physics from $2+1$ flavor domain wall QCD, Phys. Rev. D **83**, 074508 (2011).

[21] T. Blum *et al.* (RBC/UKQCD Collaboration), Domain wall QCD with physical quark masses, Phys. Rev. D **93**, 074505 (2016).

[22] P. A. Boyle, L. Del Debbio, A. Jüttner, A. Khamseh, F. Sanfilippo, and J. T. Tsang (RBC/UKQCD Collaboration), The decay constants f_D and f_{D_s} in the continuum limit of $N_f = 2+1$ domain wall lattice QCD, J. High Energy Phys. 12 (2017) 008.

[23] Y. Shamir, Chiral fermions from lattice boundaries, Nucl. Phys. **B406**, 90 (1993).

[24] V. Furman and Y. Shamir, Axial symmetries in lattice QCD with Kaplan fermions, Nucl. Phys. **B439**, 54 (1995).

[25] D. B. Kaplan, A method for simulating chiral fermions on the lattice, Phys. Lett. B **288**, 342 (1992).

[26] T. Blum and A. Soni, QCD with domain wall quarks, Phys. Rev. D **56**, 174 (1997).

[27] T. Blum and A. Soni, Domain Wall Quarks and Kaon Weak Matrix Elements, Phys. Rev. Lett. **79**, 3595 (1997).

[28] R. C. Brower, H. Neff, and K. Orginos, The Möbius domain wall fermion algorithm, Comput. Phys. Commun. **220**, 1 (2017).

[29] P. A. Boyle, L. Del Debbio, N. Garron, A. Jüttner, A. Soni, J. T. Tsang, and O. Witzel (RBC/UKQCD Collaboration), SU(3)-breaking ratios for $D_{(s)}$ and $B_{(s)}$ mesons, arXiv: 1812.08791.

[30] N. H. Christ, M. Li, and H.-W. Lin, Relativistic heavy quark effective action, Phys. Rev. D **76**, 074505 (2007).

[31] H.-W. Lin and N. Christ, Non-perturbatively determined relativistic heavy quark action, Phys. Rev. D **76**, 074506 (2007).

[32] A. X. El-Khadra, A. S. Kronfeld, and P. B. Mackenzie, Massive fermions in lattice gauge theory, Phys. Rev. D **55**, 3933 (1997).

[33] Y. Aoki, N. H. Christ, J. M. Flynn, T. Izubuchi, C. Lehner, M. Li, H. Peng, A. Soni, R. S. Van de Water, and O. Witzel (RBC/UKQCD Collaboration), Nonperturbative tuning of an improved relativistic heavy-quark action with application to bottom spectroscopy, Phys. Rev. D **86**, 116003 (2012).

[34] M. G. Alford, T. Klassen, and P. Lepage, The D234 action for light quarks, Nucl. Phys. B, Proc. Suppl. **47**, 370 (1996).

[35] A. C. Lichtl, Quantum operator design for lattice baryon spectroscopy, Ph.D. thesis, Mellon College of Science, Carnegie Mellon University, 2006, arXiv:hep-lat/0609019.

[36] A. Pochinsky, Writing efficient QCD code made simpler: QA(0), Proc. Sci., LATTICE2008 (**2008**) 040.

[37] R. G. Edwards and B. Joo (SciDAC, LHPC and UKQCD Collaborations), The Chroma software system for lattice QCD, Nucl. Phys. B, Proc. Suppl. **140**, 832 (2005).

[38] N. H. Christ, J. M. Flynn, T. Izubuchi, T. Kawanai, C. Lehner, A. Soni, R. S. Van de Water, and O. Witzel, B-meson decay constants from $2+1$-flavor lattice QCD with domain-wall light quarks and relativistic heavy quarks, Phys. Rev. D **91**, 054502 (2015).

[39] J. M. Flynn, P. Fritzsch, T. Kawanai, C. Lehner, B. Samways, C. T. Sachrajda, R. S. Van de Water, and O. Witzel (RBC/UKQCD Collaboration), The $B^*B\pi$ coupling using relativistic heavy quarks, Phys. Rev. D **93**, 014510 (2016).

[40] S. Hashimoto, A. X. El-Khadra, A. S. Kronfeld, P. B. Mackenzie, S. M. Ryan, and J. N. Simone, Lattice QCD calculation of $\bar{B} \to Dl\bar{\nu}$ decay form-factors at zero recoil, Phys. Rev. D **61**, 014502 (1999).

[41] A. X. El-Khadra *et al.*, The semileptonic decays $B \to \pi l\nu$ and $D \to \pi l\nu$ from lattice QCD, Phys. Rev. D **64**, 014502 (2001).

[42] J. Harada *et al.*, Application of heavy quark effective theory to lattice QCD. 2. Radiative corrections to heavy light currents, Phys. Rev. D **65**, 094513 (2002).

[43] C. Lehner (private communication).

[44] G. P. Lepage and P. B. Mackenzie, On the viability of lattice perturbation theory, Phys. Rev. D **48**, 2250 (1993).

[45] S. A. Gottlieb, P. B. Mackenzie, H. B. Thacker, and D. Weingarten, The $\rho^- \pi\pi$ coupling constant in lattice gauge theory, Phys. Lett. B **134**, 346 (1984).

[46] B. Efron, Bootstrap methods: Another look at the jackknife, Ann. Statist. **7**, 1 (1979).

[47] J. Flynn and C. Sachrajda (RBC Collaboration and UKQCD Collaboration), SU(2) chiral perturbation theory for K(l3) decay amplitudes, Nucl. Phys. **B812**, 64 (2009).

[48] J. Bijnens and I. Jemos, Hard pion chiral perturbation theory for $B \to \pi$ and $D \to \pi$ form factors, Nucl. Phys. **B840**, 54 (2010); **844**, 182(E) (2011).

[49] D. Bećirević, S. Prelovsek, and J. Zupan, $B \to \pi$ and $B \to K$ transitions in standard and quenched chiral perturbation theory, Phys. Rev. D **67**, 054010 (2003).

[50] R. L. Workman *et al.* (Particle Data Group), Review of particle physics, Prog. Theor. Exp. Phys. **2022**, 083C01 (2022).

[51] W. A. Bardeen, E. J. Eichten, and C. T. Hill, Chiral multiplets of heavy-light mesons, Phys. Rev. D **68**, 054024 (2003).

[52] M. Di Pierro and E. Eichten, Excited heavy-light systems and hadronic transitions, Phys. Rev. D **64**, 114004 (2001).

[53] S. Godfrey, K. Moats, and E. S. Swanson, B and B_s meson spectroscopy, Phys. Rev. D **94**, 054025 (2016).

[54] O. Lakhina and E. S. Swanson, A canonical $D_s(2317)$?, Phys. Lett. B **650**, 159 (2007).

[55] J.-B. Liu and C.-D. Lu, Spectra of heavy-light mesons in a relativistic model, Eur. Phys. J. C **77**, 312 (2017).

[56] D. Ebert, R. N. Faustov, and V. O. Galkin, Heavy-light meson spectroscopy and regge trajectories in the relativistic quark model, Eur. Phys. J. C **66**, 197 (2010).

[57] Y. Sun, Q.-T. Song, D.-Y. Chen, X. Liu, and S.-L. Zhu, Higher bottom and bottom-strange mesons, Phys. Rev. D **89**, 054026 (2014).

[58] S. Godfrey and R. Kokoski, The properties of p wave mesons with one heavy quark, Phys. Rev. D **43**, 1679 (1991).

[59] Q.-F. Lü, T.-T. Pan, Y.-Y. Wang, E. Wang, and D.-M. Li, Excited bottom and bottom-strange mesons in the quark model, Phys. Rev. D **94**, 074012 (2016).

[60] P. Colangelo, F. De Fazio, and R. Ferrandes, Bounding effective parameters in the chiral lagrangian for excited heavy mesons, Phys. Lett. B **634**, 235 (2006).

[61] H.-Y. Cheng and F.-S. Yu, Near mass degeneracy in the scalar meson sector: Implications for $B^*_{(s)0}$ and $B'_{(s)1}$ mesons, Phys. Rev. D **89**, 114017 (2014).

[62] J. M. Torres-Rincon, L. Tolos, and O. Romanets, Open bottom states and the $\bar{B}$-meson propagation in hadronic matter, Phys. Rev. D **89**, 074042 (2014).

[63] I. Woo Lee and T. Lee, Why there is no spin-orbit inversion in heavy-light mesons?, Phys. Rev. D **76**, 014017 (2007).

[64] Z.-G. Wang, Analysis of the masses and decay constants of the heavy-light mesons with QCD sum rules, Eur. Phys. J. C **75**, 427 (2015).

[65] M. F. M. Lutz and E. E. Kolomeitsev, On meson resonances and chiral symmetry, Nucl. Phys. **A730**, 392 (2004).

[66] T. Matsuki, T. Morii, and K. Sudoh, New heavy-light mesons $Q\bar{q}$, Prog. Theor. Phys. **117**, 1077 (2007).

[67] A. H. Orsland and H. Hogaasen, Strong and electromagnetic decays for excited heavy mesons, Eur. Phys. J. C **9**, 503 (1999).

[68] J. Vijande, A. Valcarce, and F. Fernandez, B meson spectroscopy, Phys. Rev. D **77**, 017501 (2008).

[69] A. M. Badalian, Yu. A. Simonov, and M. A. Trusov, The chiral transitions in heavy-light mesons, Phys. Rev. D **77**, 074017 (2008).

[70] T. A. Lahde, C. J. Nyfalt, and D. O. Riska, Spectra and M1 decay widths of heavy light mesons, Nucl. Phys. **A674**, 141 (2000).

[71] V. Dmitrašinović, Chiral symmetry of heavy-light scalar mesons with $U_A(1)$ symmetry breaking, Phys. Rev. D **86**, 016006 (2012).

[72] H.-Y. Cheng and F.-S. Yu, Masses of scalar and axial-vector B mesons revisited, Eur. Phys. J. C **77**, 668 (2017).

[73] A. F. Falk, Hadrons of arbitrary spin in the heavy quark effective theory, Nucl. Phys. **B378**, 79 (1992).

[74] R. Casalbuoni, A. Deandrea, N. Di Bartolomeo, R. Gatto, F. Feruglio, and G. Nardulli, Phenomenology of heavy meson chiral Lagrangians, Phys. Rep. **281**, 145 (1997).

[75] C. Patrignani *et al.* (Particle Data Group), Review of particle physics, Chin. Phys. C **40**, 100001 (2016).

[76] D. Arndt and C. D. Lin, Heavy meson chiral perturbation theory in finite volume, Phys. Rev. D **70**, 014503 (2004).

[77] C. Aubin and C. Bernard, Heavy-light semileptonic decays in staggered chiral perturbation theory, Phys. Rev. D **76**, 014002 (2007).

[78] C. Bernard (MILC Collaboration), Chiral logs in the presence of staggered flavor symmetry breaking, Phys. Rev. D **65**, 054031 (2002).

[79] S. Aoki *et al.* (Flavour Lattice Averaging Group), FLAG review 2019, Eur. Phys. J. C **80**, 113 (2020).

[80] J. A. Bailey *et al.* (Fermilab/MILC Collaboration), $|V_{ub}|$ from $B \to \pi\ell\nu$ decays and $(2+1)$-flavor lattice QCD, Phys. Rev. D **92**, 014024 (2015).

[81] C. W. Bernard *et al.*, The QCD spectrum with three quark flavors, Phys. Rev. D **64**, 054506 (2001).

[82] D. Giusti, V. Lubicz, C. Tarantino, G. Martinelli, F. Sanfilippo, S. Simula, and N. Tantalo, Leading isospin-breaking corrections to pion, kaon and charmed-meson masses with Twisted-Mass fermions, Phys. Rev. D **95**, 114504 (2017).

[83] C. Bourrely, B. Machet, and E. de Rafael, Semileptonic decays of pseudoscalar particles ($M \to M' + \ell + \nu_\ell$) and short distance behavior of quantum chromodynamics, Nucl. Phys. **B189**, 157 (1981).

[84] C. G. Boyd, B. Grinstein, and R. F. Lebed, Constraints on Form-Factors for Exclusive Semileptonic Heavy to Light Meson Decays, Phys. Rev. Lett. **74**, 4603 (1995).

[85] C. G. Boyd, B. Grinstein, and R. F. Lebed, Model independent determinations of $\bar{B} \to D$ (lepton), D^* (lepton) anti-neutrino form-factors, Nucl. Phys. **B461**, 493 (1996).

[86] L. Lellouch, Lattice constrained unitarity bounds for $\bar{B}^0 \to \pi^+ l\bar{\nu}_l$ decays, Nucl. Phys. **B479**, 353 (1996).

[87] C. G. Boyd and M. J. Savage, Analyticity, shapes of semileptonic form-factors, and $\bar{B} \to \pi l\bar{\nu}$, Phys. Rev. D **56**, 303 (1997).

[88] I. Caprini, L. Lellouch, and M. Neubert, Dispersive bounds on the shape of $\bar{B} \to D^{(*)}\ell\bar{\nu}$ form-factors, Nucl. Phys. **B530**, 153 (1998).

[89] M. C. Arnesen, B. Grinstein, I. Z. Rothstein, and I. W. Stewart, A Precision Model Independent Determination of $|V_{ub}|$ from $B \to \pi e\nu$, Phys. Rev. Lett. **95**, 071802 (2005).

[90] C. Bourrely, I. Caprini, and L. Lellouch, Model-independent description of $B \to \pi l\nu$ decays and a determination of $|V_{ub}|$, Phys. Rev. D **79**, 013008 (2009).

[91] A. Berns and H. Lamm, Model-independent prediction of $R(\eta_c)$, J. High Energy Phys. 12 (2018) 114.

[92] N. Gubernari, D. van Dyk, and J. Virto, Non-local matrix elements in $B_{(s)} \to \{K^{(*)}, \phi\}\ell^+\ell^-$, J. High Energy Phys. 02 (2021) 088.

[93] N. Gubernari, M. Reboud, D. van Dyk, and J. Virto, Improved theory predictions and global analysis of exclusive $b \to s\mu^+\mu^-$ processes, J. High Energy Phys. 09 (2022) 133.

[94] T. Blake, S. Meinel, M. Rahimi, and D. van Dyk, Dispersive bounds for local form factors in $\Lambda_b \to \Lambda$ transitions, arXiv:2205.06041.

[95] J. Flynn, A. Jüttner, and J. T. Tsang, Bayesian inference for form-factor fits regulated by unitarity and analyticity, arXiv:2303.11285.

[96] A. Jüttner, BFF—Bayesian Form factor Fit code https://github.com/andreasjuettner/BFF; 10.5281/zenodo.7799543 (2023).

[97] G. Duplancic and B. Melic, $B, B_s \to K$ form factors: An update of light-cone sum rule results, Phys. Rev. D **78**, 054015 (2008).

[98] A. Khodjamirian and A. V. Rusov, $B_s \to K\ell\nu_\ell$ and $B_{(s)} \to \pi(K)\ell^+\ell^-$ decays at large recoil and CKM matrix elements, J. High Energy Phys. 08 (2017) 112.

[99] R. Faustov and V. Galkin, Charmless weak B_s decays in the relativistic quark model, Phys. Rev. D **87**, 094028 (2013).

[100] W.-F. Wang and Z.-J. Xiao, The semileptonic decays $B/B_s \to (\pi, K)(\ell^+\ell^-, \ell\nu, \nu\bar{\nu})$ in the perturbative QCD approach beyond the leading-order, Phys. Rev. D **86**, 114025 (2012).

[101] R. Aaij *et al.* (LHCb Collaboration), Measurement of $|V_{cb}|$ with $B_s^0 \to D_s^{(*)-}\mu^+\nu_\mu$ decays, Phys. Rev. D **101**, 072004 (2020).

[102] Y. S. Amhis *et al.* (HFLAV Collaboration), Averages of b-hadron, c-hadron, and τ-lepton properties as of 2021, Phys. Rev. D **107**, 052008 (2023).

[103] G. Martinelli, S. Simula, and L. Vittorio, Exclusive semileptonic $B \to \pi l\nu$ and $B_s \to Kl\nu$ decays through unitarity and lattice QCD, J. High Energy Phys. 08 (2022) 022.

[104] P. del Amo Sanchez *et al.* (*BABAR* Collaboration), Study of $B \to \pi\ell\nu$ and $B \to \rho\ell\nu$ decays and determination of $|V_{ub}|$, Phys. Rev. D **83**, 032007 (2011).

[105] J. Lees *et al.* (*BABAR* Collaboration), Branching fraction and form-factor shape measurements of exclusive charmless semileptonic B decays, and determination of $|V_{ub}|$, Phys. Rev. D **86**, 092004 (2012).

[106] H. Ha *et al.* (Belle Collaboration), Measurement of the decay $B^0 \to \pi^-\ell^+\nu$ and determination of $|V_{ub}|$, Phys. Rev. D **83**, 071101 (2011).

[107] A. Sibidanov *et al.* (Belle Collaboration), Study of exclusive $B \to X_u \ell \nu$ decays and extraction of $\|V_{ub}\|$ using full reconstruction tagging at the Belle experiment, Phys. Rev. D **88**, 032005 (2013).

[108] P. Gambino, P. Giordano, G. Ossola, and N. Uraltsev, Inclusive semileptonic B decays and the determination of $|V_{ub}|$, J. High Energy Phys. 10 (2007) 058.

[109] B. O. Lange, M. Neubert, and G. Paz, Theory of charmless inclusive B decays and the extraction of V_{ub}, Phys. Rev. D **72**, 073006 (2005).

[110] J. R. Andersen and E. Gardi, Inclusive spectra in charmless semileptonic B decays by dressed gluon exponentiation, J. High Energy Phys. 01 (**2006**) 097.

[111] A. X. El-Khadra, Lattice calculation of meson form-factors for semileptonic decays, Ph.D. thesis, UCLA, 1989.

[112] D. Atwood and A. Soni, Analysis for magnetic moment and electric dipole moment form-factors of the top quark via $e^+e^- \to t\bar{t}$, Phys. Rev. D **45**, 2405 (1992).

[113] G. Isidori and O. Sumensari, Optimized lepton universality tests in $B \to V \ell \bar{\nu}$ decays, Eur. Phys. J. C **80**, 1078 (2020).

[114] J. Flynn, R. Hill, A. Jüttner, A. Soni, J. T. Tsang, and O. Witzel, Form factors for semileptonic $B \to \pi, B_s \to K$ and $B_s \to D_s$ decays, Proc. Sci., LATTICE2021 (**2022**) 306 [arXiv:2112.10580].

[115] M. Freytsis, Z. Ligeti, and J. T. Ruderman, Flavor models for $\bar{B} \to D^{(*)}\tau\bar{\nu}$, Phys. Rev. D **92**, 054018 (2015).

[116] F. U. Bernlochner and Z. Ligeti, Semileptonic $B_{(s)}$ decays to excited charmed mesons with e, μ, τ and searching for new physics with $R(D^{**})$, Phys. Rev. D **95**, 014022 (2017).

[117] U.-G. Meißner and W. Wang, $\mathbf{B_s \to K^{(*)} \ell \bar{\nu}}$, angular analysis, S-wave contributions and $|\mathbf{V_{ub}}|$, J. High Energy Phys. 01 (2014) 107.

[118] K. Nakamura *et al.* (Particle Data Group), Review of particle physics, J. Phys. G **37**, 075021 (2010).

[119] M. B. Oktay and A. S. Kronfeld, New lattice action for heavy quarks, Phys. Rev. D **78**, 014504 (2008).

[120] K. G. Chetyrkin, J. H. Kühn, and M. Steinhauser, RunDec: A Mathematica package for running and decoupling of the strong coupling and quark masses, Comput. Phys. Commun. **133**, 43 (2000).

[121] B. Schmidt and M. Steinhauser, CRunDec: A C++ package for running and decoupling of the strong coupling and quark masses, Comput. Phys. Commun. **183**, 1845 (2012).

[122] F. Herren and M. Steinhauser, Version 3 of RunDec and CRunDec, Comput. Phys. Commun. **224**, 333 (2018).

[123] D. Bigi and P. Gambino, Revisiting $B \to D \ell \nu$, Phys. Rev. D **94**, 094008 (2016).

[124] C. G. Boyd, B. Grinstein, and R. F. Lebed, Precision corrections to dispersive bounds on form-factors, Phys. Rev. D **56**, 6895 (1997).

[125] J. Grigo, J. Hoff, P. Marquard, and M. Steinhauser, Moments of heavy quark correlators with two masses: Exact mass dependence to three loops, Nucl. Phys. **B864**, 580 (2012).

[126] K. G. Chetyrkin, J. H. Kühn, A. Maier, P. Maierhofer, P. Marquard, M. Steinhauser, and C. Sturm, Charm and bottom quark masses: An update, Phys. Rev. D **80**, 074010 (2009).

[127] A. Bazavov *et al.*, Staggered chiral perturbation theory in the two-flavor case and SU(2) analysis of the MILC data, Proc. Sci., LATTICE2010 (**2010**) 083 [arXiv:1011.1792].

[128] K. Cichy, E. Garcia-Ramos, and K. Jansen, Chiral condensate from the twisted mass Dirac operator spectrum, J. High Energy Phys. 10 (**2013**) 175.

[129] C. Alexandrou, A. Athenodorou, K. Cichy, M. Constantinou, D. P. Horkel, K. Jansen, G. Koutsou, and C. Larkin, Topological susceptibility from twisted mass fermions using spectral projectors and the gradient flow, Phys. Rev. D **97**, 074503 (2018).

[130] S. Borsányi, S. Dürr, Z. Fodor, S. Krieg, A. Schafer, E. E. Scholz, and K. K. Szabó, SU(2) chiral perturbation theory low-energy constants from $2+1$ flavor staggered lattice simulations, Phys. Rev. D **88**, 014513 (2013).

[131] S. Dürr *et al.* (Budapest-Marseille-Wuppertal Collaboration), Lattice QCD at the physical point meets SU(2) chiral perturbation theory, Phys. Rev. D **90**, 114504 (2014).

[132] P. A. Boyle *et al.*, Low energy constants of SU(2) partially quenched chiral perturbation theory from $N_f = 2+1$ domain wall QCD, Phys. Rev. D **93**, 054502 (2016).

[133] G. Cossu, H. Fukaya, S. Hashimoto, T. Kaneko, and J.-I. Noaki, Stochastic calculation of the dirac spectrum on the lattice and a determination of chiral condensate in $2+1$-flavor QCD, Prog. Theor. Exp. Phys. **2016**, 093B06 (2016).

[134] S. Aoki, G. Cossu, H. Fukaya, S. Hashimoto, and T. Kaneko (JLQCD Collaboration), Topological susceptibility of QCD with dynamical Möbius domain-wall fermions, Prog. Theor. Exp. Phys. **2018**, 043B07 (2018).

[135] S. Narison, QCD parameter correlations from heavy quarkonia, Int. J. Mod. Phys. A **33**, 1850045 (2018); **33**, 1892004(A) (2018).